

REPORT SERIES IN AEROSOL SCIENCE  
N:o 198 (2017)

On the solar radiative effects of atmospheric ice and dust

Päivi Pauliina Haapanala

Division of Atmospheric Sciences  
Department of Physics  
Faculty of Science  
University of Helsinki  
Helsinki, Finland

Academic dissertation

*To be presented, with the permission of the Faculty of Science  
of the University of Helsinki, for public criticism in auditorium E204,  
Gustaf Hällströmin katu 2a, on 2 June 2017, at 12 o'clock noon.*

**Helsinki 2017**

Author's Address: Department of Physics  
P.O. Box 64  
FI-00014 University of Helsinki  
paivi.haapanala@helsinki.fi

Supervisors: Docent Timo Nousiainen, Ph.D.  
Finnish meteorological institute  
Helsinki, Finland

Docent Petri Räisänen, Ph.D.  
Finnish meteorological institute  
Helsinki, Finland

Reviewers: Docent Antti Arola, Ph.D.  
Finnish meteorological institute  
Kuopio, Finland

Associate Research Professor David Mitchell, Ph.D.  
Desert Research Institute  
Reno, Nevada, USA

Opponent: Senior scientist Piet Stammes, Ph.D.  
Royal Netherlands Meteorological Institute  
De Bilt, Netherlands

ISBN 978-952-7091-80-7

ISSN 0784-3496

Helsinki 2017

Unigrafia Oy

ISBN 978-952-7091-81-4

<http://ethesis.helsinki.fi>

Helsinki 2017

Helsingin yliopiston verkkojulkaisut

## Acknowledgments

The research for this thesis was carried out at the Department of Physics of the University of Helsinki. I wish thank the former and present heads of the department, Prof. Juhani Keinonen and Prof. Hannu Koskinen, for providing work facilities. I have had the opportunity to do scientific research at the Division of Atmospheric Science and at the Division of Astronomy and Geophysics, for that I'm grateful to Profs. Markku Kulmala and Hannu Koskinen. During the many years of working with this thesis (2010–2017), thanks to our flexible working environment, I have been able to be in parental leave for a period that sums up to almost three years. I acknowledge the Academy of Finland, the Finnish Center of Excellence in Atmospheric Science—From Molecular and Biological Processes to the Global Climate, and Maj and Tor Nessling Foundation for the financial support. I appreciate the time and valuable comments of the two pre-examinors of this thesis, Docent Antti Arola and Prof. David Mitchell.

I am indebted to my supervisors Docents Timo Nousiainen and Petri Räisänen for their continuous guidance, support and sharing their knowledge on radiative effects of atmospheric ice and dust with me. Particularly, I wish to thank Timo for introducing me the light scattering phenomena and for endless support and interest toward my work especially in the beginning of my Ph.D. I'm grateful for Petri's super precise eye for finding errors in my work and after that also solutions for them. I would like to show my gratitude towards Greg M. McFarguhar for providing me data on in situ measured ice crystals and for being the unofficial third supervisor for me. From him I have learned a great deal about microphysical properties of ice crystals and tried to learn the scientific writing style. Michael Kahnert and all my other co-authors are acknowledged for their research ideas, advices and positive feedbacks. I wish to thank colleagues at the Division of Atmospheric science, especially those who have made the coffee and lunch breaks pleasant with funny scientific and unscientific discussions. Colleagues in Dynamic meteorology group are thanked for introducing other fields of meteorology to me. I'm grateful for Hannakaisa Lindqvist, Mari Pihlatie, Annakaisa von Leber and Dmitri Moisseev for work and non-work related conversations and support.

Finally, I thank my extended family and friends for their encouragement and for releasing my mind out of work. I am really grateful for having a clever and loving husband who has shared my interest towards meteorology. I appreciate his willingness to stay on parental leave to enable me to finish my thesis.

Päivi Pauliina Haapanala  
University of Helsinki, 2017

## **Abstract**

Both atmospheric ice and mineral dust are considered to play important roles in our climate system through their impacts on the radiative energy budget. These impacts depend on the size, shape, composition and concentration of the ice and dust particles. These particles are often non-spherical with a variety of different regular and irregular shapes. The non-spherical shape yields uncertainties in our understanding of how these particles interact with radiation as their optical properties cannot be accurately calculated using spherical model particles (i.e., Mie theory). One of the main aims of this work is to better understand the impact of particle shape on radiative effects of ice and dust. Another aim is to investigate the relation between size distributions of ice and dust particles and radiative effects. For dust particles, the overall goal is to improve the treatment of optical properties of dust in global aerosol-climate models.

In this thesis, the optical properties for variously shaped ice and dust particles are obtained from pre-existing databases. The single-scattering properties of each particle class are integrated over either measured or assumed size-shape distributions to obtain the ensemble-averaged optical properties. The vertical profiles of ensemble-averaged optical properties are used as input to radiative transfer models. Different radiative transfer models, atmospheric and surface properties etc. are used in this work, based on the requirements of each studied case. For ice clouds, the simulated radiances or irradiances are compared against ground-based observations. The sensitivity of a global aerosol-climate simulations to dust particle nonsphericity is also investigated.

This thesis offers a broad outlook on the effects of ice clouds on the direct, diffuse, and total shortwave irradiances as well as on the angular dependence of the circumsolar radiance. In addition, it offers interesting new insight into understanding the connection between particle morphology, cloud microphysics and cloud radiative effects. It is found that both irradiances and circumsolar radiances are sensitive to the concentration of small ice crystals, which is highly uncertain due to limitations in measurement techniques. Comparison of simulated and measured radiation in the presence of ice clouds suggests that most natural ice crystals are not pristine, but can either have some surface roughness or other non-idealities in their shapes. The papers related to dust particles reveal that the use of a carefully validated shape model of spheroids, which presents the asymmetry parameter of dust better than spheres, has only small or moderate impacts on regional and global-scale direct radiative effects of dust. Consistent with this, experiments with a global aerosol-climate model indicate that the

assumption of spherical shape for dust particles is not a considerable error source in climate simulations. Most probably, however, this conclusion cannot be extended to remote sensing applications.

Keywords: ice crystal, mineral dust, single-scattering properties, shortwave radiation, circumsolar radiation, radiative transfer modeling, spheroids

# Contents

<b>1</b>	<b>Review of papers and the author's contribution</b>	<b>5</b>
<b>2</b>	<b>Introduction</b>	<b>8</b>
2.1	Background . . . . .	8
2.2	Objectives and scopes . . . . .	10
<b>3</b>	<b>Theory</b>	<b>12</b>
3.1	Optical properties . . . . .	14
3.2	Radiative transfer equation . . . . .	17
<b>4</b>	<b>Atmospheric ice and dust particles</b>	<b>21</b>
4.1	Ice crystals . . . . .	21
4.2	Mineral dust particles . . . . .	24
<b>5</b>	<b>Computational tools</b>	<b>28</b>
5.1	Databases of optical properties . . . . .	28
5.2	Radiative transfer models . . . . .	29
5.2.1	LibRadtran . . . . .	29
5.2.2	MC-UniK . . . . .	30
5.3	Aerosol-climate model ECHAM5.5-HAM2 . . . . .	31
<b>6</b>	<b>Optical properties of ice crystals and mineral dust aerosols</b>	<b>33</b>
6.1	Derivation of ensemble-averaged optical properties . . . . .	33
6.1.1	Ice cloud . . . . .	33
6.1.2	Mineral dust . . . . .	37
6.2	Examples of the ensemble-averaged optical properties . . . . .	39
<b>7</b>	<b>Results</b>	<b>45</b>
7.1	Shortwave radiation in the presence of ice clouds . . . . .	45
7.1.1	Impact of small ice crystals on radiative fluxes . . . . .	46
7.1.2	Comparison of modeled and observed radiative fluxes . . . . .	46
7.1.3	Impact of ice crystal properties on circumsolar radiance . . . . .	48

7.1.4	Comparison of modeled and observed circumsolar radiances . . .	50
7.2	Impact of dust particle nonsphericity on radiation . . . . .	53
7.2.1	Local shortwave radiative impacts . . . . .	53
7.2.2	Global climate impacts . . . . .	56
<b>8</b>	<b>Conclusions</b>	<b>60</b>
	<b>References</b>	<b>63</b>

## List of publications

This thesis consists of an introductory review, followed by four research articles. In the introductory part, these papers are cited according to their roman numerals. Papers I, III, and IV are reprinted under the John Wiley and Sons license numbers 4086430618613, 4086430217551, and 4086420800115, respectively. Paper II is reprinted under the Creative Commons License. It is noted that the family name of the candidate has changed from Mauno to Haapanala during the process.

- I** Mauno, P., McFarquhar, G. M., Räisänen, P., Kahnert, M., Timlin M. S., and Nousiainen, T. (2011). The influence of observed cirrus microphysical properties on shortwave radiation: a case study over Oklahoma. *J. Geophys. Res.*, **116**, D22208, doi:10.1029/2011JD016058.
- II** Haapanala, P., Räisänen, P., McFarquhar, G. M., Tiira J., Macke, A., Kahnert, M., DeVore J., and Nousiainen, T. (2016). Disk and circumsolar radiances in the presence of ice clouds. *Atmos. Chem. Phys. Discuss.*, doi:10.5194/acp-2016-967. Accepted for publication in *Atmos. Chem. Phys.*.
- III** Haapanala, P., Räisänen, P., Kahnert, M., and Nousiainen, T. (2012). Sensitivity of the shortwave radiative effect of dust on particle shape: comparison of spheres and spheroids *J. Geophys. Res.*, **117**, D08201. doi:10.1029/2011JD017216.
- IV** Räisänen, P., Haapanala, P., Chung, C. E., Kahnert, M., Makkonen., R., Tonttila, J., and Nousiainen, T. (2013). Impact of dust particle nonsphericity on climate simulations. *Q. J. R. Meteorol. Soc.*, **139**, 2222–2232. doi:10.1002/qj.2084.

# 1 Review of papers and the author's contribution

**Paper I** explores the possibility to model shortwave radiative fluxes with a radiative transfer model based on in-situ measured size-shape distributions of ice crystals. The airborne microphysical data were combined with existing databases of wavelength-dependent single-scattering properties of ice crystals to obtain vertical profiles of optical properties. This study expanded upon past studies examining cloud radiative interactions by clearly quantifying the distinct impact of uncertainties in the concentration and shape of small ice crystals on radiative fluxes. The results revealed that concentrations of small ice crystals can strongly influence the fluxes. Furthermore, this study highlighted the need of a consistent definition of direct and diffuse radiation in calculations and observations. Since the instruments measuring direct solar radiation cover an angular range of a few degrees around the center of Sun, the contribution to diffuse downward radiation from this region has to be added to the modeled direct radiation and subtracted from the modeled diffuse radiation. Finally, it was found that reducing asymmetry parameter by a factor of less than 10% could improve the agreement between simulations and measurements. This reduction could be associated with the presence of surface roughness, air bubble inclusion or other non-idealities in ice crystals.

The author was responsible for conducting the radiative transfer simulations with the LibRadtran radiative transfer model and for writing most of the paper. She also prepared the model input and did the comparison of measured and modeled fluxes. All figures, except those in the Appendix, were made by the author.

**Paper II** compares radiative transfer simulations and measurements of disk and circumsolar radiances within an opening angle of  $16^\circ$  around the center of the Sun. The question of how much light do ice crystals scatter in near forward-directions, raised by **Paper I**, is investigated here. This work extends and supports the previous studies on the impact of ice crystals' properties on near-forward scattering by modeling radiances instead of irradiances and by conducting a large amount of systematic sensitivity tests using realistic, measurement-based description of atmospheric, aerosol and ice crystals properties. To quantify the sensitivity of the radiances to crystal properties such as shape and roughness, simulations were carried out with different single-habit distributions in addition to the in-situ derived shape distributions using three roughness options for the crystals. Ice crystal roughness (or more generally, non-ideality) was

found to be the most important parameter influencing the circumsolar radiance, ice crystal sizes and shapes also playing a significant role. When comparing to radiances measured with the ground-based instrument, rough ice crystals tend to reproduce the observed radiances better than idealized smooth ice crystals.

The author designed, together with co-authors, the required modifications of the Monte Carlo radiative transfer model, which she then implemented. She combined the in situ data and single-scattering properties of ice crystals from a pre-existing database and conducted all the radiative transfer simulations. The author was responsible for analyzing results and producing the figures, except Figure 2, and for writing the paper together with Petri Räisänen.

**Paper III** investigates the sensitivity of local shortwave direct radiative effects (DRE) of dust to particle nonsphericity. Simulations with the LibRadtran radiative transfer model were conducted using optical properties of either spherical dust particles or different shape distributions of spheroidal dust particles. It was found that the impacts of nonsphericity on the radiative effects of dust are non-systematic. They depend largely on the shape distribution and whether the mass or optical thickness are conserved when comparing to spherical particles. In addition, results for different distributions of spheroids might deviate more from each other than from those for spheres. For the mass-conserving case, it was found that the impacts on radiative fluxes are small. For example, when using a shape distribution of spheroids that favors strongly elongated spheroids, the DRE at the surface differs at most 5% from that for spherical particles in the mass-conserving case. This stems from compensating shape related effects on optical thickness and asymmetry parameter. However, in the optical thickness conserving case, the DRE at the surface can be up to 15% smaller for spheroids than spheres. Based on this study it is not immediately obvious that using spheroidal dust particles in climate simulations instead of spheres would lead to significantly different results.

The author was responsible for computing the optical properties of different size-shape distributions of spherical and spheroidal dust particles by using an existing Mie calculation algorithm and database of optical properties of dust. She also conducted all the model simulations, produced the figures and wrote the paper in collaboration with co-authors.

**Paper IV** concludes the research started in **Paper III** by testing the impact of dust particle shape in a global aerosol-climate model, ECHAM5.5-HAM2. It was the first-

ever climate simulation with non-spherical dust particles. The optical properties of dust particles were modeled using one of the ensembles of spheroids used in **Paper III**. In the first experiments, the effect of dust nonsphericity on solar radiative fluxes was evaluated diagnostically. It was found that in the volume-to-area conserving case (which is very close to the optical thickness conserving case considered in **Paper III**), the shortwave radiative effect of insoluble dust was 16% smaller than that for spheres, mainly because spheroids feature a larger asymmetry parameter (i.e., less backward scattering) than spheres. In the mass-conserving case the differences were smaller due to the compensating nonsphericity effects on dust optical depth, single-scattering albedo and asymmetry parameter. In the second experiment, the effect of dust nonsphericity on climate simulated by ECHAM5.5-HAM2 was investigated interactively. It was found that in global climate simulations, it is probably safe to neglect the impact of nonsphericity of dust, presuming that spheroidal dust particles do describe the optical properties of dust correctly.

The author's contribution was to provide the look-up tables of optical properties of spherical and spheroidal dust particles needed for ECHAM5.5-HAM2. A total of twelve look-up tables needed to be generated for this work. She also commented on the manuscript.

## 2 Introduction

### 2.1 Background

Solar radiation is the only significant source of energy for the Earth-atmosphere system. Almost all of the energy radiated by the Sun and incident on the top of the atmosphere is shortwave (SW) radiation at wavelengths between  $0.1 \mu\text{m}$  and  $4 \mu\text{m}$ . This radiation contains 5–8% of ultraviolet (UV) radiation and the remainder is almost evenly distributed between visible light and near-infrared radiation (Deland et al., 2004). Atmospheric circulation and thereby weather and climate are driven by the uneven distribution of absorbed solar energy. However, on average, the Earth is nearly in a radiation balance: the amount of incident solar radiation absorbed by the atmosphere and surface is balanced by a nearly-equal amount of longwave radiation emitted back to space. Even small changes in this planetary radiation balance can cause changes in the climate. To be able to describe the interactions of the atmosphere with radiation, it is essential that its composition including aerosols and cloud particles is known. These interactions depends both on the properties of the radiation (wavelength and polarization) and particle (size, shape, and refractive index) (Baran, 2012; Nousiainen, 2009; Petty, 2006; Liou, 2002). Actually, most of the light that we see does not come directly from its source but indirectly by the process of scattering. Some of the scattering processes happening in the atmosphere can be even observed with naked eye: molecular scattering by atmospheric gases colors the sky blue, scattering inside water droplets can produce rainbows and scattering inside ice crystals create impressive halos.

The composition of the atmosphere varies depending on the location, season, time of the day and weather. The atmosphere is composed of various gases, solid and liquid particles such as aerosols, water droplets, snow flakes and ice crystals. From the aerosol types, sea salt and mineral dust particles are the most abundant ones in the atmosphere. It has been suggested that mineral dust originating from Sahara exerts the largest local and global direct radiative effect of all aerosol species (Haywood et al., 2003). To determine the direct radiative impacts of dust particles, their concentrations, size-shape distributions and chemical compositions which vary depending on the source area should be known (Sokolik et al., 2001; Nousiainen, 2009; Durant et al., 2009; Otto et al., 2011; Yi et al., 2011). In addition to dust, ice crystals are known to be

important components in the local and global radiation balance through their role in the redistribution of radiative energy (Baran, 2012; Stephens et al., 1990). The basic shape of an ice crystal is most often hexagonally symmetric, but it may vary depending on the atmospheric states under which it grows. Several habit classes have been defined to describe the observed shapes of ice crystals. Optical properties of these various habit classes are under intensive investigation (Macke, 1993; Macke et al., 1996; Yang and Liou, 1998; Yang et al., 2000, 2003; Chen et al., 2006; Borovoi et al., 2007; Um and McFarquhar, 2007, 2009; Baran, 2009; Um and McFarquhar, 2011; Yang et al., 2013, e.g) Ice clouds, which can cover extensive areas of the Earth’s surface at any given time, are composed of ice crystals. The optical properties and further the radiative impacts of ice clouds can be highly variable given the high variability in the microphysical properties of ice crystals (Macke et al., 1998; McFarquhar et al., 1999, 2002; Baran et al., 2004; Schlimme et al., 2005; Schmitt and Heymsfield., 2007; Baran, 2009, 2012; Yang et al., 2013). The microphysical and single-scattering properties of ice and dust particles cannot be assumed to be known exactly (Um and McFarquhar, 2011; Um, 2015; Fridlind et al., 2016; Nousiainen, 2009; Durant et al., 2009). The remaining large uncertainties in the ensemble averaged optical properties of dust and ice are reflected in uncertainties in their radiative effects (Baran, 2009, 2012; Durant et al., 2009; Colarco et al., 2014).

The radiation balance at the surface can be quantified by using a selection of ground-based instruments, for example direct radiation can be measured with a pyrheliometer and the upward and downward radiative fluxes with shaded pyranometers and pyrgeometers. However, due to the technique used to measure direct radiation, it can also include some portion of solar radiation originating from a small disk around the sun, circumsolar radiation. There have been some efforts to quantify the amount of circumsolar radiation in the measured direct radiation in the presence of an ice cloud and to account for its impact on the underestimation of cloud optical thickness (Shiabara et al., 1994; Kinne et al., 1997; Segal-Rosenheimer et al., 2013). For example Segal-Rosenheimer et al. (2013) proposed a new approach to derive ice cloud optical thickness and effective diameter from sun photometry measurements by using ice-cloud optical property models. The circumsolar radiance or irradiance can also be measured with the Sun and Aureole measurement (SAM) system (DeVore et al., 2009). The SAM data also holds potential for retrieving properties (e.g., size distributions) of aerosols and ice crystals. Most direct observations of particle size distribution and other microphysical properties are, of course, obtained from in situ measurements from aircraft. Ground-

based radars and lidars together with satellite measurements, however, can provide better spatial and temporal coverage than in situ measurements. These instruments can detect and quantify precipitation, cloud properties and coverage, dust plumes, and surface properties (e.g. albedo). From radar, lidar and satellite observations properties such as optical thickness and particle size distributions can be retrieved. To be able to interpret the measurements from these instruments, knowledge of the single-scattering properties of atmospheric gases and particles is important. Depending on the application, ice and dust particles can be either targets whose properties are to be measured, or objects interfering with the measurement of another target. In both cases, it is essential to know how they interact with electromagnetic radiation.

## 2.2 Objectives and scopes

The investigations in this thesis are focused on the shortwave direct radiative effects. Atmospheric ice crystals and mineral dust aerosols are selected for examination because their non-spherical and often irregular shape yields uncertainties and difficulties in predicting their interactions with radiation. While the shape of particles also influences the transfer of longwave radiation (although in general, not as strongly as solar radiation), the impact of shape on longwave optical properties of ice and dust particles is not considered in this study. Dust also has indirect radiative effects through its impacts on clouds and precipitation, but these are also beyond the scope of the present thesis. The aim of this thesis was to pursue knowledge of:

- What is the impact of the concentration and morphology of small ice crystals on cloud radiative properties and SW radiation? (**Paper I**)
- How sensitive is the circumsolar radiation to ice cloud characteristics such as ice crystal size, shape and non-ideality? And conversely, can circumsolar radiation reveal properties of ice crystals? (**Paper II**)
- Compared to spherical model particles, how much do the optical properties of spheroidal dust particles impact the simulated shortwave radiative effects of dust. (**Paper III**)
- What is the role of the size equivalence on the differences between shortwave radiative effects of spheroidal and spherical dust particles? (**Paper III and IV**)

- How large an error source for climate simulations is the use of spherical model particles to calculate the optical properties of dust particles? To which extent is this dependent on the size equivalence? (**Paper IV**)

These questions have been investigated using three different radiative transfer models and carefully validated optical properties of ice crystals and mineral dust aerosols. The shapes of the dust particles are described with shape distributions of spheres and spheroids and corresponding optical properties are used as input to either stand-alone SW radiative transfer models or climate model SW radiation calculations. The size distributions of ice crystals are based on aircraft in situ measurements and they are combined either with in-situ-based habit distributions or single-habit distributions to study the impacts of ice crystal habit on SW radiation. A number of sensitivity tests are carried out to quantify the impacts and uncertainties related to microphysical properties of ice and dust and to those related to external conditions such as time of the day and properties of the underlying surface. In the dust investigations the author strove to improve the accuracy of radiative impact estimations with direct applicability to climate modeling. In this thesis, the solar radiative transfer in the atmosphere in the presence of either ice (**Papers I and II**) or dust particles (**Paper III and IV**) is investigated. Both broadband fluxes (**Papers I, III–IV**) and monochromatic radiances (**Paper II**) are simulated with radiative transfer models. **Paper IV** deals not only with the solar radiative effects of dust, but also the ensuing climatic impacts in climate model simulations.

### 3 Theory

The analysis of a radiation field in the atmosphere often requires the consideration of the amount of radiation confined to an element of solid angle. The differential solid angle in the polar coordinate system, which is often used in radiative transfer modeling, can be written

$$d\Omega = \sin(\theta)d\theta d\phi, \quad (1)$$

where  $\theta$  and  $\phi$  are the zenith and azimuth angles (Figure 1). Units of the solid angle are expressed in terms of the steradian (*sr*).

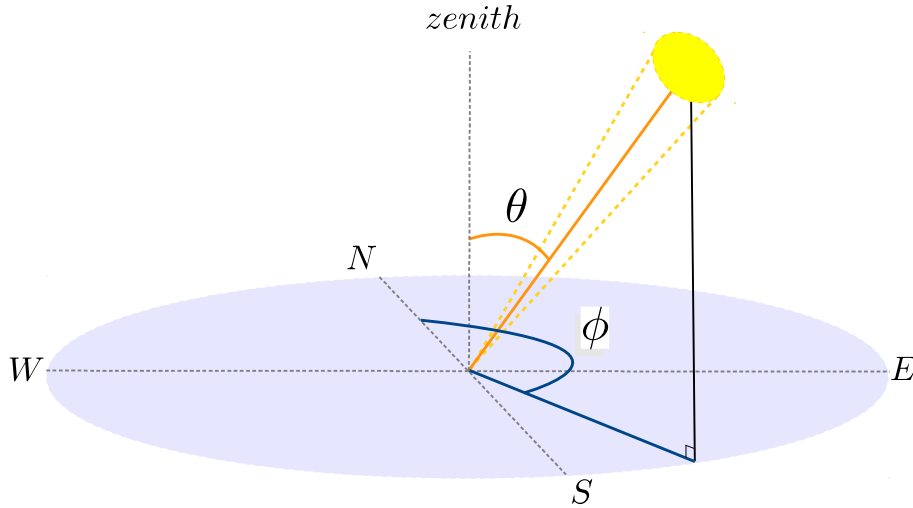


Figure 1: Schematic representation of the solar zenith  $\theta$  and azimuth  $\phi$  angles.

The amount of radiation at a wavelength  $\lambda$  coming from a certain solid angle onto some arbitrary perpendicular surface is called (monochromatic) radiance or intensity and it can be expressed as

$$I_\lambda = \frac{dE_\lambda}{\cos(\theta)d\Omega d\lambda dt dA}, \quad (2)$$

The unit of the radiance is energy ( $E$ ) per area ( $A$ ) per time ( $t$ ) per wavelength and per steradian and in this thesis it is given in  $\text{Wcm}^{-2}\mu\text{m}^{-1}\text{sr}^{-1}$ . Another relevant quantity is the irradiance, also referred to as the radiative flux, which has the units of power per area (integrated over solid angles):

$$F_\lambda = \int I_\lambda \cos(\theta) d\Omega \quad (3)$$

and in polar coordinates

$$F_\lambda = \int_0^{2\pi} \int_0^{\pi/2} I_\lambda(\theta, \phi) \cos(\theta) \sin(\phi) d\theta d\phi. \quad (4)$$

These quantities can be defined either as monochromatic (one wavelength) or broadband (spectrally integrated). They are often examined either on a plane perpendicular to incident radiation or on a horizontal plane such as the top of the atmosphere (TOA) or the surface of the Earth ( $z_0$ ). The difference between these two planes depends on the cosine of solar zenith angle,  $\mu = \cos(\theta)$ , which further depends on the latitude, day of the year and time of the day.

For calculations of solar radiative transfer in the atmosphere, the upper boundary condition is provided by the incident solar radiation at the TOA. The incident solar radiation depends on the solar constant (which has a mean broadband value of  $S_0=1361 \text{ Wm}^{-2}$  (Kopp and Lean, 2011) but varies slightly depending on the solar activity), the Earth-Sun distance (which depends on the day of the year) and  $\mu$ . Thus, the incident solar radiation is not uniformly distributed on the Earth, but depends strongly on the location, season and time of day. In most radiative transfer applications, it is sufficient to treat the Sun as a point source, but in some applications, it is essential to take into account the finite width of the solar disk. An example of the latter is the calculation of circumsolar radiation in **Paper II**. In that paper, Sun is treated as a disk with a diameter of  $0.532^\circ$  as observed from the ground, and the variations in intensity within the disk are accounted for using a formula given by Böhn-Vitense (1989). These variations arise because the solar radiation reaching the observer on Earth originates in the photosphere of the Sun, peaking at an optical depth of roughly unity along the line of sight. On average, this corresponds to a temperature of about 5778 K. However, along a line of sight toward the Sun's limb, an optical depth of one is reached at a higher altitude with a lower temperature. Hence the intensity reaching us from the limb of the Sun is lower than that from the center (Green and Jones, 2015).

The atmospheric gas molecules, cloud particles and aerosols can interact with electromagnetic radiation by scattering, absorbing and emitting it. The interactions depend both on the properties of the particles (such as composition, size, and shape) and on the properties of the radiation (wavelength and polarization state). The solution to light scattering phenomena starts from the Maxwell equations that describe the properties of the radiation by relating the electric and magnetic fields together (e.g. Jackson, 1999; Bohrem and Hufman, 1983). Further, the properties of radiation can be characterized

by using the Stokes vector  $S = [I, Q, U, V]$ . The elements of this vector are called the Stokes parameters. The first element,  $I$ , is the intensity and the other elements,  $Q$ ,  $U$ , and  $V$ , describes the polarization state of the radiation. Polarization is important for example for radar observations of precipitation, but most often in the atmospheric radiative transfer calculations it can be neglected without introducing large errors to radiances or fluxes and thus it is beyond the scope of this thesis.

### 3.1 Optical properties

Next, the interactions between particles and radiation are described using optical properties relevant from the shortwave radiative transfer modeling point of view. The wavelength-dependent single-scattering properties describe how one particle interacts with radiation. In the atmosphere, there is always a mixture of different molecules and particles with different single-scattering properties. To be able to describe their interactions with radiation, volume-averaged optical properties are needed. These are also referred to as bulk-optical properties or ensemble-averaged optical properties. The single-scattering properties depend on the properties of the particles (e.g size, shape and composition) and on the wavelength of the radiation. The ensemble-averaged optical properties depend also on the concentration of particles. An important quantity in determining how particles interact with radiation is the complex refractive index  $m = n + ik$ , which characterizes the particles response to the time varying electromagnetic field. It depends both on the composition of the particle and on the wavelength of the radiation. The real part of refractive index,  $n$ , describes the speed of light in vacuum compared to the speed of light in the medium, and the imaginary part,  $k$ , quantifies the relative amount of energy absorbed by the medium. The scale of the particle size relative to the incident wavelength is described with the dimensionless size parameter:

$$x = \frac{2\pi r}{\lambda}, \quad (5)$$

where  $r$  is the radius of a sphere. For nonspherical particles the particle size is not unambiguous, but various measures of size can be used, such as, for example, the maximum dimension  $D_{\max}$  or the effective radius  $r_{\text{eff}}$ . Another widely-used option for ice crystal size is the use of the volume-to-projected area effective diameter:

$$D_{\text{eff}} = \frac{3V}{2P}, \quad (6)$$

where  $V$  is the volume (at bulk density) and  $P$  the projected area of a particle or particle ensemble (Bryant and Latimer, 1969; Mitchell and Arnott, 1994; Mitchell, 2002). The size parameter and the refractive index together dictate the nature of scattering, and therefore, they are essential to the choice of a suitable method for calculating single-scattering properties. For different size parameters, different kind of solutions for calculating the interaction with radiation can be used. For  $x \ll 1$  Rayleigh scattering and for  $x \gg 1$  geometric optics methods can be used. For the particles and wavelengths considered in thesis, the sizes of the particles are much larger than the wavelength of radiation, leading to size parameters much larger than unity. The calculation of the optical properties of spherical dust particles in **Papers III** and **IV** were done by the author using an existing computational code based on the Lorenz-Mie theory. With the Mie solution to Maxwell's equations, an exact and analytic solution of the optical properties of a sphere is obtained. For complex and irregular particle shapes, no analytical solution exists for calculating the scattering properties. The focus of this thesis has not been in the computational methods of single-scattering properties; rather, the single-scattering properties of individual ice crystals and spheroidal dust particles have been obtained from pre-calculated databases of optical properties (see Sect. 5.1). In these databases the optical properties are given as a function of shape and either the size parameter or particle size and wavelength. Next, the obtained single-scattering properties relevant for this thesis are introduced. All these properties are functions of wavelength, but for convenience of notation, the wavelength dependence is not marked explicitly.

The total power removed from the incident radiation by the particle is described by its extinction cross section,  $C_{\text{ext}}$ . This quantity can be divided into energy scattered and absorbed by the particle

$$C_{\text{ext}} = C_{\text{sca}} + C_{\text{abs}}, \quad (7)$$

where  $C_{\text{sca}}$  and  $C_{\text{abs}}$  are the scattering and absorption cross sections. The extinction cross section equals the area perpendicular to radiation that would be needed to collect the amount of power removed from the incident radiation. Further, the scatterer's efficiency to extinct, absorb and scatter energy per area can be described by

$$Q_{\text{ext}} = \frac{C_{\text{ext}}}{G}, Q_{\text{abs}} = \frac{C_{\text{abs}}}{G}, Q_{\text{sca}} = \frac{C_{\text{sca}}}{G}, \quad (8)$$

where  $Q_{\text{ext, abs, sca}}$  are the extinction, absorption and scattering efficiencies and  $G$  is the geometric cross section of the particle. For a spherical particle  $G = \pi r^2$ . The relative

contribution of scattering and absorption is described with the single-scattering albedo,

$$\omega = \frac{C_{\text{sca}}}{C_{\text{ext}}}. \quad (9)$$

The single-scattering albedo varies from 0 to 1, unity referring to a nonabsorbing particle.

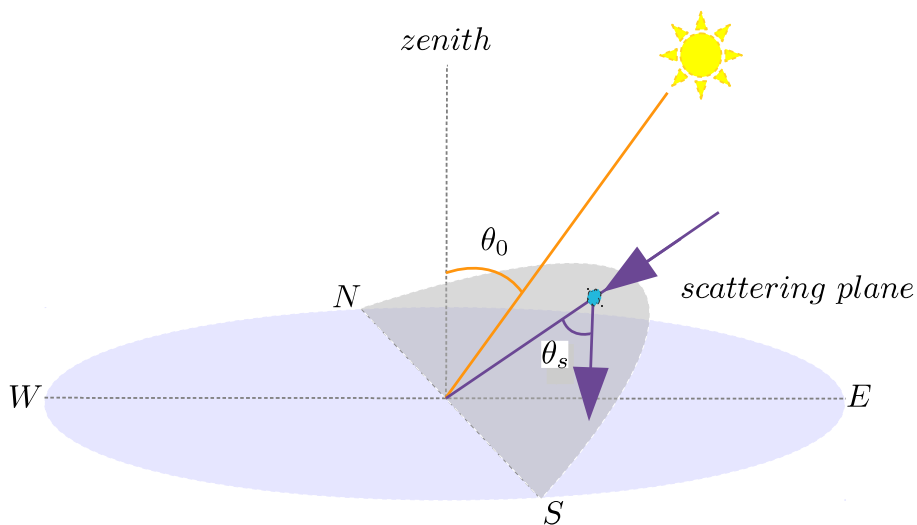


Figure 2: Schematic representation of the scattering angle  $\theta_s$  between the incident and scattered radiation in the scattering plane (shaded area).

A three-dimensional scattering process is often solved in the so-called scattering plane. The scattering plane is a plane defined by the propagation directions of the incident and scattered radiation. For a given scattering plane, the angular dependence of scattered intensity for unpolarized light can be described by a phase function  $P_{11}(\theta_s)$ , which is normalized such that

$$1/2 \int_0^\pi P_{11}(\theta_s) \sin(\theta_s) d\theta_s = 1, \quad (10)$$

where the scattering angle  $\theta_s$  is the angle between incident and scattered directions of propagation in the scattering plane (Figure 2). In this case, the phase function describes the likelihood of scattering to occur in a direction  $\theta_s$ . In some applications of radiative transfer, the phase function can be replaced by a single number, the asymmetry parameter  $g$ . It equals the mean value of the cosine of scattering angle, weighted by the phase function:

$$g = 1/2 \int_0^\pi P_{11}(\theta_s) \sin(\theta_s) \cos(\theta_s) d\theta_s. \quad (11)$$

Thus, asymmetry parameter is a measure of the preferred scattering direction: When forward scattering ( $< 90^\circ$ ) dominates over backward scattering  $0 < g < 1$  and when the opposite is true  $-1 < g < 0$ . In nature, however,  $g < 0$  appears rarely if ever.

Extinction due to, for example, a cloud layer including several particles with different shapes and sizes, is described by the volume extinction coefficient,  $K_{\text{ext}}$ . It is obtained by integrating  $C_{\text{ext}}$  of individual particles with concentrations  $n(D, s)$  over their sizes  $D$  and shapes  $s$ :

$$K_{\text{ext}} = \iint C_{\text{ext}}(D, s)n(D, s)dDds \quad (12)$$

Similarly, the volume scattering coefficient describes scattering due to several particles:

$$K_{\text{sca}} = \iint C_{\text{sca}}(D, s)n(D, s)dDds. \quad (13)$$

Values of  $K_{\text{ext}}$  and  $K_{\text{sca}}$  of different cloud layers or a cloud layer and molecular scatterers are additive and can be summed together. From  $K_{\text{ext}}$  the optical thickness ( $\tau$ ) of that volume or a layer (ensemble) can be calculated. The optical thickness of a whole cloud or atmosphere can be calculated from the vertical profile of  $K_{\text{ext}}$ :

$$\tau_z = \int_{z_b}^{z_t} K_{\text{ext}}(z)dz, \quad (14)$$

where  $z_b$  and  $z_t$  are the lower and upper bounds of the layer, respectively. The ensemble-averaged single-scattering albedo of the particles within the unit volume is given by

$$\omega = \frac{K_{\text{sca}}}{K_{\text{ext}}}. \quad (15)$$

The ensemble averaged phase function is :

$$P_{11} = \frac{\iint P_{11}(D, s)C_{\text{sca}}(D, s)n(D, s)dDds}{\iint C_{\text{sca}}(D, s)n(D, s)dDds}. \quad (16)$$

Further the ensemble-averaged asymmetry parameter is:

$$g = \frac{\iint g(D, s)C_{\text{sca}}(D, s)n(D, s)dDds}{\iint C_{\text{sca}}(D, s)n(D, s)dDds}. \quad (17)$$

## 3.2 Radiative transfer equation

In the atmosphere, the horizontal and vertical distributions of the wavelength-dependent ensemble-averaged optical properties affect the radiation. Usually the vertical gradient is much larger than the horizontal. To be able to describe how the direct

and diffuse radiation travels through the atmosphere, the radiative transfer equation (RTE) is needed. This equation states that during its propagation in the atmosphere, radiation is subject to losses due to extinction and to gains due to scattering and emission from other directions to the direction of propagation. The radiative transfer equation for monochromatic radiance  $I(s, \theta, \phi)$  in the atmosphere can be given qualitatively as

$$\frac{dI(s, \theta, \phi)}{ds} = -\text{extinction} + \text{scattering} + \text{emission}, \quad (18)$$

where  $s$  is the location, and  $\theta$  and  $\phi$  the zenith angle and azimuth angle of the direction of propagation. RTE is a function of the location, direction, wavelength, and time. In order to determine  $I(s, \theta, \phi)$  at a particular location, the scattering and emission from all directions must be determined simultaneously. In general, this problem cannot be solved analytically, and numerical (and most often approximate) techniques are needed. The two approaches to solve the radiative field employed in this thesis are briefly introduced in Sect. 5.2. More detailed information about these approaches and other existing computational techniques to solve RTE accurately and efficiently can be found from e.g. Liou (2002).

Next a more specific form of the radiative transfer equation is introduced. The optical depth measured from the top of the atmosphere ( $\tau$ ) is used as the vertical coordinate and  $\mu \equiv \cos(\theta)$  is used to specify the direction of propagation of the radiation. If the atmosphere is divided into vertical layers which are assumed to be horizontally homogeneous and Earth's curvature is neglected (the plane-parallel approximation) and hence no dependence of horizontal coordinates is taken into account, the SW radiative transfer equation following Liou (2002) can be expressed as:

$$\mu \frac{dI(\tau, \theta, \phi)}{d\tau} = I - J, \quad (19)$$

where  $J$  is the source function for scattering:

$$J = \frac{\omega}{4\pi} \int I(\tau, \theta', \phi') P_{11}(\theta, \phi, \theta', \phi') d\theta' d\phi' + \frac{\omega}{4\pi} S_0 P_{11}(\theta, \phi, \theta_0, \phi_0) e^{-\tau \mu_0^{-1}}, \quad (20)$$

where  $\theta, \phi$  and  $\theta', \phi'$  are zenith and azimuth angles of incident and scattered radiation,  $S_0$  is the solar constant,  $\theta_0$  the solar zenith angle, and  $\mu_0 = \cos(\theta_0)$ . The first term on the right hand side represents the scattering of diffuse radiation from all other directions to the direction of interest  $(\theta, \phi)$ , and the second term the scattering of direct solar radiation. One simplification is to use an azimuthally averaged radiative

transfer equation. By skipping a few definitions and derivations we can rewrite Eq. (19) as

$$\mu \frac{dI(\tau, \mu)}{d\tau} = I(\mu) - \frac{\omega}{2} \int_{-1}^1 I(\tau, \mu') P_{11}(\mu, \mu') d\mu' - \frac{\omega}{4\pi} S_0 P_{11}(\mu, -\mu_0) e^{-\tau \mu_0^{-1}}, \quad (21)$$

where the positive  $\mu$  denotes the upward and negative  $\mu$  the downward propagating radiation.

The aim of solving the RTE is to obtain the radiative quantities such as radiance or irradiance (radiative flux) at some arbitrary surface. Once the monochromatic radiances are solved, monochromatic irradiances can be obtained by integrating the radiances over the upper and lower hemisphere. Finally, broadband irradiances are obtained by integrating the monochromatic irradiances over the solar spectral region.

Both equations (19) and (21) describe only the scattered part of the radiation and the direct radiation can be derived by the simple Beer-Bouguer-Lambert law of extinction:

$$F_{dir}^{\downarrow}(\tau) = \mu_0 S_0 e^{-\tau \mu_0^{-1}} \quad (22)$$

The total downward flux at any level in the atmosphere is simply the sum of the direct and diffuse downward fluxes. Furthermore, a key term of the surface energy budget is the surface net radiation, which is the difference between incoming and outgoing radiative fluxes at the surface:

$$F_{SW}^{net}(\tau) = F_{dir}^{\downarrow}(\tau) + F_{diff}^{\downarrow}(\tau) - F_{diff}^{\uparrow}(\tau). \quad (23)$$

To obtain the upwelling flux at the surface  $F_{diff}^{\uparrow}$ , the reflectance of the surface needs also to be set. Often the surface is assumed to be a Lambertian reflector, which reflects equal amounts of radiation to all directions.

The direct radiative effect (DRE) of dust is defined as the difference between net fluxes of dusty and dust-free atmospheres. Similarly, the cloud radiative effect (CRE) of an ice cloud is the difference between net fluxes of cloudy and cloud-free atmospheres (clear sky). For simplicity, in the following equations DRE and CRE are used as synonyms yet CRE is used in cloud studies instead of DRE. At the surface, the SW direct radiative effect can be expressed as:

$$DRE_{z_0} = [F_{z_0}^{net}]_{dusty/cloudy} - [F_{z_0}^{net}]_{clear\ sky}. \quad (24)$$

At the top of the atmosphere (TOA), where  $F_{\text{diff}}^{\downarrow}$  is always zero and  $F_{\text{dir}}^{\downarrow}$  is the same for both dusty or cloudy and clear skies, the SW direct radiative effect simplifies to the difference between clear and dusty or cloudy sky diffuse upward fluxes

$$DRE_{TOA} = [F_{\text{diff}}^{\uparrow}]_{\text{clear sky}} - [F_{\text{diff}}^{\uparrow}]_{\text{dusty/cloudy}}. \quad (25)$$

A negative DRE at the TOA indicates cooling of the surface-atmosphere system as a whole, whereas a negative DRE at the surface indicates cooling of the surface. The direct radiative effect on the atmospheric absorption is

$$DRE_{ABS} = [F_{TOA}^{net} - F_{z_0}^{net}]_{\text{dusty/cloudy}} - [F_{TOA}^{net} - F_{z_0}^{net}]_{\text{clearsky}} = DRE_{TOA} - DRE_{z_0}. \quad (26)$$

In summary, atmospheric radiative transfer models are used to solve the radiation field and its interactions with the atmosphere (trace gases, aerosols, and/or clouds) and surface. In these models the atmosphere is usually divided into horizontally homogeneous layers. For each layer the wavelength-dependent ensemble-averaged single-scattering albedo, phase function, and volume extinction coefficient need to be determined. In addition, accurate knowledge of the solar constant, solar zenith angle and surface reflectance are required as input to the models. As output from the models, radiances, irradiances and/or heating rates are obtained. Broadband results are obtained by numerically integrating (or summing) the monochromatic results over the wavelength region.

## 4 Atmospheric ice and dust particles

### 4.1 Ice crystals

A significant fraction of the atmospheric cloud particles are ice crystals. These crystals can be found in mixed-phase and ice clouds. Ice clouds, such as cirrus and contrails, are located high in the troposphere at altitudes around 6–12 km. At these altitudes the temperature is low ( $T < -30^\circ\text{C}$ ) and therefore the clouds are composed almost completely of ice crystals. These clouds may appear to be transparent and look thin, but actually their vertical extent can exceed even 2 km. Satellite observations indicate that ice clouds cover approximately one third of the earth at any given time (Wylie and Menzel, 1999; Wylie et al., 2005; Stubenrauch et al., 2010). In the tropics, the coverage can be even 60% (Wylie et al., 2005; Stubenrauch et al., 2010). Spatial coverage of ice clouds and their ability to interact with radiation makes them an important component of Earth’s radiation balance. Their radiative effects are highly variable depending on their spatial coverage, temporal frequency and, of course, on their microphysical characteristics such as ice crystal size, habit and concentration (Kinne et al., 1997; Zhang et al., 1999; Buschmann et al., 2002; Schlimme et al., 2005; Wendisch, 2005, 2007; Boudala et al., 2007; McFarquhar et al., 2007; Baran, 2009, 2012; Zhou et al., 2012; Yi et al., 2013). The uncertainty about the radiative properties of ice clouds largely follows from an inadequate understanding of their microphysical behavior.

Ice crystals form through heterogeneous nucleation around suitable freezing nuclei (Hoose and Möhler, 2012) or by freezing of supercooled water or haze droplets under temperatures lower than  $-35$ – $-40^\circ\text{C}$  (Herbert et al., 2015; Koop et al., 2000). These processes are not yet fully understood. After ice nucleation, only small crystals can be spherical, larger ones varying from compact to more complex shapes and often aggregated shapes. The basic form of ice crystals is most often hexagonal which is due to the molecular structure of atmospheric ice (Macke, 1993). Yet, the shapes can vary from symmetric pristine hexagonal plates, columns, and single bullets to bullet rosettes, non-symmetric aggregates and irregular shapes (e.g. Baran, 2012, and the references therein). The shape of an ice crystal is affected by the temperature, pressure and supersaturation conditions as well as by the vertical motion and turbulence the crystal experiences (Bailey and Hallet, 2003; Mason, 1992). In addition, the growth rates of different ice crystal shapes may vary because of the diffusional or collisional processes.

These conditions may vary during the lifetime of an ice crystal, leading to a weak correlation between the ambient conditions and the crystal shape. In mid-latitudes, cirrus are often composed of bullet rosette- and column-shaped ice crystals and their sizes can vary from less than ten micrometers up to few thousand micrometers (Heymsfield et al., 2002; Schmitt and Heymsfield., 2007). As also noted in **Paper I**, larger crystals tend to inhabit the lower part of the cloud while small crystals are often found at the top of the cloud (Baran, 2009, 2012). Ice crystals may contain internal inclusions such as air bubbles or particles (e.g. soot) or they can have distortions and rough surfaces. These non-idealities can have a large impact on the optical properties and further on the radiative effects of ice clouds (Macke et al., 1996; Labonnete et al., 2001; Wendisch, 2005, 2007; Baran, 2009; Baum et al., 2010; Baran, 2012; Um and McFarquhar, 2011; Yi et al., 2013; Yang et al., 2013; Cole et al., 2014; Ulanowski et al., 2014).

Information about the shapes of ice crystals can be obtained from images taken by optical array probes installed on a measurement aircraft. Since these images capture only the projected area of the crystals, they do not reveal the real three-dimensional shape. Cloud Particle Imager (CPI) is one of the probes used to measure ice crystal habit and it has a higher resolution (nominally  $2.3 \mu\text{m}$ ) than the previously used instruments. However, also this instrument can only be used to confidently identify the shape of large ice crystals ( $D > 50 \mu\text{m}$ ) as Um and McFarquhar (2011) and Ulanowski et al. (2004) show that its limited image resolution and blurring of images due to diffraction renders the shape classification of small ice crystals unreliable. Because CPI has a small and poorly defined sample volume it cannot be used to determine reliable size distributions, but it can be used to determine the fractional size-dependent habit distributions. Few examples of CPI images that reveal the variety of ice crystal shapes are shown in 3. Due to the large range of ice crystal sizes, a collection of instruments is needed to measure the size distribution. However, even for these instruments, small and poorly defined sample volumes (Baumgardner et al., 1997; McFarquhar et al., 2016) cause uncertainties in the measurement of the size distribution of small ice crystals. Potential contributions from remnants of larger ice crystals shattered on the shroud, inlet and tips of probes (e.g. Gardiner and Hallett, 1985; McFarquhar et al., 2007; Korolev et al., 2011, 2013) also reduce the reliability of concentrations and size distributions of small ice crystals. This artificial shattering may have been a problem with the Forward Scattering Spectrometer Probe (FSSP) used in **Paper I**. Instruments used in **Paper II** had better tips that decreased the amount of particle shattering. Despite the large uncertainties in the shapes and concentrations of small ice crystals (Korolev et al., 2011,

2013; McFarquhar et al., 2016), it has been suggested that they make a significant contribution to the optical properties and further to the radiative effects of ice clouds (Boudala et al., 2007; McFarquhar et al., 2007). In addition to CPI, the Desert Research Institute (DRI) replicator Hallet et al. (1976) and the Video Ice Particle Sampler (VIPS, McFarquhar and Heymsfield (1997) have been used to characterize the shape of ice crystals. Based on the observations it has been assumed that small ice crystals are quasi-spherical. For example McFarquhar and Heymsfield (1997); Korolev et al. (2003); Nousiainen and McFarquhar (2004); Nousiainen et al. (2011) have suggested that the shape of crystals smaller than  $60 \mu\text{m}$  could be quasi-spherical. In radiative transfer simulations and in other applications the shape of small crystals have been presented for example by spheres, Gaussian random spheres, droxtals and Chebyshev particles (McFarquhar et al., 2002; Nousiainen and McFarquhar, 2004; Nousiainen et al., 2011). In the study of Um and McFarquhar (2011), a new idealized model, the budding Bucky ball, that resembles the small ice analogue was developed. The Chebyshev particle, Gaussian random sphere, droxtal and budding Bucky ball shape models look all similar when imaged by the CPI. However, Um and McFarquhar (2011) noted that there are significant differences in scattering between these shape models.



Figure 3: Examples of ice crystals measured by Cloud Particle Imager (CPI) installed on a measurement aircraft.

The optical properties of ice crystals cannot be accurately described using spherical model particles (Mie theory) as can be done for liquid water droplets. The role of the ice crystal shapes and sizes on their optical properties (Macke, 1993; Macke et al., 1996, 1998; Yang and Liou, 1998; Yang et al., 2000; McFarquhar et al., 2002; Yang et al., 2003; Schmitt and Heymsfield., 2007; McFarquhar et al., 2007; Um and McFarquhar, 2007, 2009; Baum et al., 2010; Um and McFarquhar, 2011; Yang et al., 2013) and further on the shortwave radiative effects of ice clouds (Takana and Liou, 1989, 1995; Zhang et al., 1999; McFarquhar et al., 1999; Schlimme et al., 2005; Baran, 2012) have been studied in much detail. The effects of crystal orientation on the optical properties is also investigated (Borovoi et al., 2016, 2007; Chen et al., 2006). The studies of Segal-Rosenheimer et al. (2013) and Reinhardt et al. (2014) have revealed that differences in the modeled forward scattering of smooth and roughened ice crystals as well as different shape distributions of ice crystals lead to differences in the circumsolar radiation. DeVore et al. (2012) also noted the impact of ice crystals properties (roughness and effective radius) on calculated circumsolar radiances. In addition, several studies have developed alternative parameterizations of ice clouds that can be employed in climate models (Ebert and Curry, 1992; Fu, 1996; Fu et al., 1998). Despite these and a number of other investigations, significant uncertainties still remain in the size and shape distributions of ice crystals, their single-scattering properties, and further in their impact on SW radiation and climate.

## 4.2 Mineral dust particles

Atmospheric mineral dust particles are one of the most abundant aerosol specie in the atmosphere. It has been suggested that they have the largest local and global direct radiative effect of all aerosol species (Haywood et al., 2003). Mineral dust particles impact the climate not only by interacting with radiation but also, for example, by acting as ice nuclei (Teller, 2012) and fertilizing soils. Through these mechanisms, dust also has important indirect radiative effects. These particles are wind drifted from deserts and arid regions, from which Sahara and Gobi deserts are the largest source areas (Middleton et al., 2001; Prospero et al., 2002). Depending on the atmospheric conditions and on the properties of the dust particles, dust can be wind-transported over long distances and stay in the atmosphere from hours to weeks before gravitational settling (dry deposition) or rainout (wet deposition). The direct and indirect effects of mineral dust may change in the future due to climate warming and land use changes.

The composition of dust particles is often inhomogeneous (Chou et al., 2008) and their shapes are exclusively irregular, varying from compact and rounded shapes to flakes, fibers and aggregates (Kanler et al., 2009). Some examples of dust particle shapes imaged with electro-microscope are shown in Figure 4 and the chemical compositions of an dust particle is illustrated in Figure 5. In addition to the overall shape, surface roughness is considered a major challenge in mineral dust modeling (Nousiainen, 2009). Their sizes varies from nanometers to even hundreds of micrometers. The large temporal variability of atmospheric dust particle concentrations are easy to image when comparing a clear day and dust storm; however the concentrations also vary within a single dust plume as a result of wet and dry deposition. The mineralogical and chemical compositions of atmospheric dust reflect those of the source area (Claquin et al., 1999), and to some extent, particles can be back-tracked to a certain area. This, however, is not straightforward as they can be mixed with particles from other sources.

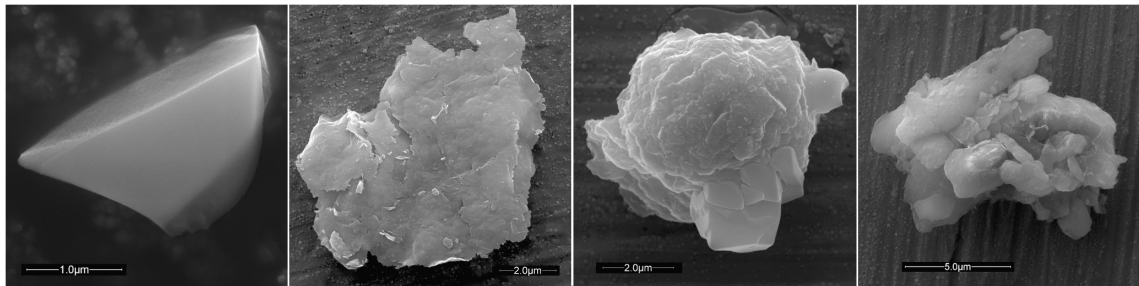


Figure 4: Electro-microscopy images of mineral dust particle shapes. (Courtesy of Timo Nousiainen and Konrad Kandler)

Although mineral dust has been studied much, there are still large uncertainties in the microphysical properties including size-shape distributions, concentrations, chemical and mineral compositions (Chou et al., 2008; Kanler et al., 2009). These uncertainties propagate to uncertainties in the complex refractive index and in simulating the optical properties and radiative effects of mineral dust (Sokolik et al., 2001; Kahnert and Kylling, 2004; Kahnert, 2004; Yang et al., 2007; Otto et al, 2009; Durant et al., 2009; Feng et al., 2009; Nousiainen, 2009; Wiegner et al., 2009; Otto et al, 2011; Merikallio et al., 2011; Yi et al., 2011; Wagner et al., 2012; Kempainen et al., 2015; Nousiainen and Kandler, 2015). For example, Kempainen et al. (2015) showed that the optical properties of single dust particles depended significantly on their internal structures.

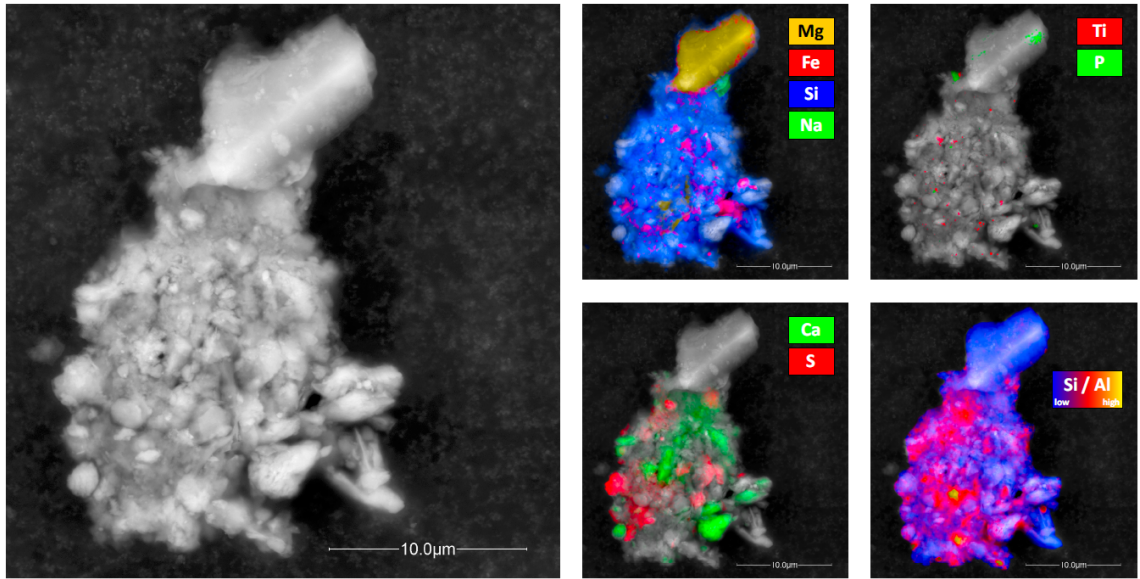


Figure 5: An example of the in-homogeneity of mineral dust particle. (Courtesy of Timo Nousiainen and Konrad Kandler)

The consideration of the nonsphericity of mineral dust is important for remote sensing applications, radiative transfer modeling and possible also for climate modeling. Recently, considerable efforts have been made to quantify the error caused by modeling optical properties of these nonspherical particles using Mie theory (which is only valid for isotropic, homogeneous spheres) (Kahnert et al., 2007; Yang et al., 2007; Nousiainen, 2009; Yi et al., 2011; Colarco et al., 2014; Nousiainen and Kandler, 2015). Various in situ, remote sensing and laboratory measurements reveal that scattering of visible light by dust particles differs significantly from that based on spherical model particles (Kahnert, 2004; Nousiainen et al., 2006; Nousiainen, 2009; Yi et al., 2011; Merikallio et al., 2011; Nousiainen and Kandler, 2015). A number of studies (Mishchenko et al., 1997; Kahnert and Kylling, 2004; Nousiainen et al., 2006; Dubovik et al., 2006; Otto et al., 2009; Merikallio et al., 2011; Wagner et al., 2012) indicate that model particles as simple as spheroids can reproduce the optical properties of dust particles significantly better than spheres. The impact of using spheroids instead of spheres on remote sensing applications have been investigated e.g. by Feng et al. (2009). While real-world dust particles are neither spheres, spheroids or ellipsoids, these model particles are used in light scattering modeling. Nousiainen et al. (2011) show that a shape distribution of spheroids that best reproduces the optical properties of a non-spheroidal particle

may not represent in any way its shape. Wiegner et al. (2009) also show that observed aspect ratio distributions appear to be clearly different. Following Nousiainen et al. (2006), the shape of a spheroid can be expressed by a shape parameter,

$$\xi = \begin{cases} b/a - 1 & a \leq b \text{ (oblate)} \\ 1 - a/b & a > b \text{ (prolate)}, \end{cases} \quad (27)$$

where  $a$  is the diameter of the spheroid along its main symmetry axis, and  $b$  the maximum diameter in the orthogonal direction. Compared to a sphere, the geometry of a spheroid is characterized using only one additional parameter, the aspect ratio. Otto et al (2009) found that instead of spheres, volume equivalent oblate spheroids with an axis ratio of 1:1.6 lead to the best agreement with their lidar, Sun photometer and scanning electron microscope field measurements of Saharan dust. They also noted that the use of a distribution of aspect ratios would be an interesting alternative to using a constant aspect ratio. The shape distribution of spheroids can be parameterized as

$$f(\xi, n) = C|\xi^n|, \quad (28)$$

where  $C$  is a normalization coefficient such that the integral over all considered shape parameters  $\xi$  equals unity, and  $n$  is a free parameter that defines the form of the shape distribution. The size distribution of mineral dust is often described using log-normal size distribution and effective radius,  $r_{\text{eff}}$ .

## 5 Computational tools

In the radiative transfer simulations of this thesis, the ice crystals or dust particles are described as vertical profiles of ensemble-averaged optical properties. Section 5.1 described the pre-calculated databases of optical properties of ice and dust used in this work. After that in Section 6.2, the radiative transfer and climate models for which the optical properties were used as input are introduced.

### 5.1 Databases of optical properties

The cross-sectional area and single-scattering properties ( $Q_{\text{ext}}$ ,  $\omega$ , and  $g$  or  $P_{11}$ ) of individual ice crystals used in **Paper I** were obtained from several sources: the database of Yang et al. (2000) for plates, solid columns, planar bullet rosettes composed of four branches, spatial bullet rosettes composed of six branches, and rough aggregates, the database of Yang et al. (2003) for droxtals, the study of McFarquhar et al. (2002) for Chebyshev particles and unpublished data by Timo Nousiainen for Gaussian random spheres. In **Paper II**, the optical properties were obtained from the updated version of Ping Yang’s database (Yang et al., 2013), which provides data for nine habits: plate, hexagonal column, hollow column, solid bullet rosette, hollow bullet rosette, 8-element column aggregate, 5-element plate aggregate, 10-element plate aggregate, and droxtal. In these databases the single-scattering properties are provided as a function of wavelength, particle’s maximum dimension (hereafter  $D$ ) and shape. Furthermore, the database of Yang et al. (2013) provides three roughness options for each habit: completely smooth (CS), moderately rough (MR), and severely rough (SR). The effect of roughness is simulated by randomly distorting the surface slope for each incident ray, assuming a normal distribution of local slope variations with a standard deviation of 0, 0.03 and 0.50 for the CS, MR and SR cases (Eq. 1. in Yang et al. (2013)). In fact, this treatment does not represent any specific roughness characteristics but attempts instead to mimic the effects due to non-ideal crystal characteristics in general (roughness effects, irregularities and inhomogeneities like air bubbles). These sources of single-scattering properties use several validated methods to calculate the single-scattering properties. For example Yang et al. (2000) employs improved geometric ray-tracing computational method, finite difference time-domain (FDTD) technique (Yang and Liou, 1996) and for more complex geometries ray-by-ray/Monte Carlo technique (Yang and Liou, 1997). Yang et al. (2013) employs Amsterdam Discrete Dipole

Approximation (Yurkin et al., 2007) for small particles (size parameters smaller than about 20) and improved geometric optics (Yang and Liou, 1998; Bi et al., 2009) for large particle.

The optical properties of spheroidal dust particles are from the database of Dubovik et al. (2006). The database, provides the single-scattering properties for a size-shape distributions of spheroidal particles with complex refractive index  $m$ . The shape distribution need to be given with the shape parameters  $\xi$ , and the size distribution with  $r_{\text{eff}}$  and  $\sigma$ . The database of Dubovik et al. (2006) is based on numerically exact T-matrix method (Mishchenko et al., 1994) and modified geometric optics approximation (Yang and Liou, 1996) calculations of single-scattering properties of polydisperse, randomly oriented homogeneous spheroidal particles. Even though the latter method is not exact, according to Yang et al. (2007) the asymmetry parameters it provides agree well with those obtained from an exact method.

## 5.2 Radiative transfer models

In most cases, an accurate solution of the radiative transfer equation is too time-consuming and simplifications are needed in radiative transfer modeling. One commonly used simplifying assumption is that of a plane-parallel horizontally homogeneous atmosphere, which is also assumed in this thesis. It means that Earth’s curvature is neglected, that the atmospheric properties including those of aerosols and clouds vary only in the vertical direction, and that no three-dimensional radiative transfer effects are accounted for. Based on Buschmann et al. (2002), the plane parallel approximation for relatively homogeneous (e.g. non-convective) mid-latitude cirrus most likely does not induce flux errors larger than 10%. For the radiative transfer models, the vertical profiles of the studied atmospheres (including ice or dust) are described using ensemble-averaged optical properties, i.e.  $\tau$  or  $K_{\text{ext}}$ ,  $\omega$ , and  $P_{11}$  or  $g$ .

### 5.2.1 LibRadtran

In **Papers I** and **III**, the freely available LibRadtran software package; a library of radiative transfer routines and programs (Mayer and Kylling, 2005; Emde et al., 2016) was used. The libRadtran is a suite of tools for radiative transfer calculations in the Earth’s atmosphere and it can be used to compute radiances and irradiances in the

solar and terrestrial part of the spectrum. Its main tool is the `uvspec` program. The `uvspec` offers a selection of several radiative transfer solvers from which the DIScrete Ordinate Radiative Transfer (DISORT) solver by Stamnes et al. (1988) was chosen to be used in **Papers I** and **III**. DISORT is perhaps the most widely used method to solve the radiative transfer equation. In both **Papers I** and **III**, 16 streams for angular discretization of the radiance field were used. The spectral resolution of the calculations can be chosen from the five different options offered by LibRadtran: spectrally resolved calculations, band parameterization, line-by-line calculations, correlated- $k$  method, or pseudo-spectral calculations. Spectrally resolved calculations were used for wavelengths shorter than 791 nm (780 nm) in **Paper I** (**Paper III**), while for longer wavelengths, the Kato et al. (1999) correlated  $k$ -distribution method was used. This parametrization covers the solar spectral range (0.24 to 4.6  $\mu\text{m}$ ) with 32 spectral bands and includes 575 subbands in total (Kato et al., 1999). The radiative transfer solver DISORT produces three different irradiances: Direct downward, diffuse downward and diffuse upward. In **Papers I** and **III**, these irradiances are solved both at the top of the atmosphere and at the surface.

LibRadtran provides the six standard Air Force Geophysics Laboratory (AFGL) atmospheric constituent profile files by Anderson et al (1986). From these the 'U.S standard' atmospheric profile was used in **Paper I** to extend the vertical profiles of pressure, temperature, and humidity obtained from radiosoundings up to the top of the atmosphere as well as to provide profiles of  $\text{O}_3$ ,  $\text{O}_2$ ,  $\text{CO}_2$  and  $\text{NO}_2$  throughout the atmosphere. In **Paper III**, the 'tropical model' atmospheric profile was used for molecular scattering and absorption, except that the water vapor content was halved to roughly account for the dry conditions typically prevailing in regions with abundant mineral dust.

### 5.2.2 MC-UniK

MC-UniK is the forward Monte Carlo Model of the University of Kiel by Macke et al. (1999) for efficient calculations of radiances at discrete directions. The model has been validated within the Intercomparison of 3-D-Radiation Codes project (Cahalan et al., 2005). In **Paper II**, a modified version of it was used to simulate the angular dependence of solar disk and circumsolar radiances. Even though a plane-parallel, horizontally homogeneous atmosphere was assumed in the radiative transfer calculations of paper **II**, the Monte Carlo technique was applied instead of DISORT because of

its flexibility. Specifically, it allows to consider the finite width of the solar disk and to compute radiances at an arbitrarily high angular resolution in the vicinity of the direction of the Sun, without incurring extreme computational costs.

In MC-Unik, the path of photons is traced from their source (i.e., the incoming solar radiation at the TOA) through the atmosphere until they are reflected back to space or absorption makes the weight of the photons negligible. The Monte Carlo method is a stochastic approach, in which the results contain random errors, the magnitude of which decreases with an increasing number of photons. In **Paper II**, 8 million photons were used in each simulation. Mc-UniK simulates the scattering events of photons within the atmosphere using a non-truncated treatment for the phase functions. The free path length is based on Beer’s law and gives the distance between two successive scattering processes. The scattering direction is derived using a random number generator so that the scattering angle  $s$  corresponding to a given random number  $[0,1]$  equals the cumulative phase function from 0 to  $s$ , and the azimuth angle is sampled uniformly in the range  $[0, 2\pi]$ . Absorption is taken into account by multiplying the photon weight by the local single-scattering albedo. For reasons of computing time and variance reduction, techniques as proposed by Barker et al. (2003) have been implemented. Mc-UniK employs the Local Estimate Method (e.g., Marshak and Davis, 2005) which is more efficient for calculating the radiance field than the common Monte Carlo photon counting method because no photons get lost. Thus, in effect, MC-UniK assumes that a fraction of the photon is scattered directly into each detector at each scattering process. These photons are attenuated along the optical path between the scattering location and the detector.

In **Paper II**, the author modified the original MC-UniK, in which the Sun is treated as a point source, to account for the finite width of the solar disk including the limb darkening effect (Böhm-Vitense, 1989). For the half opening angle of the Sun a value of  $0.267^\circ$  was used. In addition, the model output was modified to include the direct and diffuse radiances at the surface (in units of  $\text{Wcm}^{-2}\mu\text{m}^{-1}\text{sr}^{-1}$ ) for specified detector positions.

### 5.3 Aerosol-climate model ECHAM5.5-HAM2

ECHAM is a family of atmospheric general circulation models developed by the Max Planck Institute for Meteorology. The original ECHAM model branched from an early

release of the ECMWF (European Centre for Medium Range Weather Forecasts) model to enable climate studies (Simmons et al., 1989). From the ECHAM family the global aerosol–climate model ECHAM5.5-HAM2 (Roeckner et al., 2003, 2006) coupled to a mixed-layer ocean model was used in **Paper IV**. It was run at a horizontal resolution of T42 (300 km) with 19 levels in the vertical and with a 30 minute time step.

HAM2 (Zhang et al., 2012) is an updated version of the aerosol model HAM (Stier et al., 2005). When coupled with ECHAM5.5, it predicts the evolution of an aerosol ensemble with five internally and externally mixed compositions: dust, sea salt, black carbon, sulphate, and particulate organic matter. The model HAM2 uses the aerosol dynamics module M7 (Vignati et al., 1994), which represents the size distribution of aerosols through a superposition of seven log-normal modes: nucleation, Aitken soluble, Aitken insoluble, accumulation soluble, accumulation insoluble, coarse soluble, and coarse insoluble. The size distributions of the modes are described using log-normal size distributions with standard deviation  $\sigma_g = 1.59$  for the nucleation, Aitken and accumulation modes and with  $\sigma_g = 2.0$  for the coarse modes. The number median radius of the particles is  $0.05 \mu\text{m} < r_m < 0.5 \mu\text{m}$  for the accumulation modes and  $r_m > 0.5 \mu\text{m}$  for the coarse modes, for example. Each of the modes has its own look-up table (LUT) for the aerosol optical properties. In standard HAM2, the LUTs have been precomputed based on the Mie theory. In **Paper IV**, new LUTs based on the spheroidal shape assumption were implemented for the accumulation insoluble and coarse insoluble modes, in which dust appears as the only chemical component. Dust also appears as a part of the accumulation soluble and coarse soluble modes, where it is assumed to be internally mixed with other aerosol components. These modes and the three remaining modes were treated as spheres in **Paper IV**. In the atmosphere, dust can be removed by dry and wet deposition and transferred from insoluble to soluble modes through coagulations and condensation (Stier et al., 2005).

For climate model purposes, a rigorous solution of the radiative transfer equation to obtain the fluxes is computationally too expensive. Thus, simplifications and parameterizations are needed. The SW radiative transfer of ECHAM5.5 follows Fouquart et al. (1980). The scheme uses the delta-Eddington approximation for the scattering and includes Rayleigh scattering, absorption by water vapor and ozone, and  $CO_2 + N_2O + CO + CH_4 + O_2$  as a uniformly mixed gas. Aerosols and cloud particles are effected by absorption and scattering. The scheme has four spectral bands, one for the UV+visible range and three for the near-infrared range.

## 6 Optical properties of ice crystals and mineral dust aerosols

This section is divided into two parts. First, Section 6.1 describes how the ensemble-average optical properties employed in this thesis were derived from the observed size-shape distributions of ice crystals and from the assumed size-shape distributions of dust particles. Second, examples of the derived optical properties and how they depend on the assumed particle properties are shown in Section 6.2. These are introduced to set the stage for discussing the radiative transfer and climate modeling results in Section 7, where they act as important input parameters.

### 6.1 Derivation of ensemble-averaged optical properties

#### 6.1.1 Ice cloud

In both **Papers I** and **II**, the ensemble-averaged optical properties of ice clouds (and atmospheric gases and aerosols) needed as input to the radiative transfer models were based on data obtained at the Atmospheric Radiation Measurement (ARM) program's Southern Great Plains (SGP) site in the north central Oklahoma, USA. The measurements used in **Paper I** were carried out during the spring 2000 Cloud Intensive Operational Period (IOP) campaign and in **Paper II** during the year 2010 Small PARTICles in Cirrus (SPARTICUS) campaign. The IOP was the first-ever effort to document the three-dimensional cloud field from observational data, whereas SPARTICUS concentrated on the impact of small ice crystals and to obtain better statistics on cirrus cloud microphysical properties. During IOP, the University of North Dakota (UND) Citation aircraft sampled ice clouds on five research flights on four different days. During SPARTICUS, the Stratton Park Engineering Company (SPEC) Inc. Learjet 25 aircraft conducted 101 missions sampling many ice clouds. Both Citation and Learjet 25 housed a suite of microphysical probes that measured the size and shape distributions of ice crystals, bulk water contents and state parameters during the flights. The measurement times and corresponding altitude ranges of the flight profiles studied in this theses are shown in Table 1. These flight profiles were deemed suitable for our investigations as there was a visually observable ice cloud without lower cloud layers and all the needed in situ and ground-based measurement data had good quality. The

ground-based radiation measurements suggested that the ice cloud on 13 March 2000 was the most long-lived and homogeneous among the five different flights of the spring 2000 IOP. In **Paper I**, the two flight legs of that day (a ramped horizontal ascent and a descent spiral) were used to assess the relative importance of assumptions about the size and shape distributions of small ice crystals ( $D < 120 \mu\text{m}$ ) on radiative fluxes. These legs are henceforth named flight A and B. In **Paper II**, ramped horizontal flight legs measured on 23 March 2010 (flight A in **Paper II**, but hereafter flight C) and 24 June 2010 (flight B in **Paper II**, but hereafter flight D) were investigated. Based on the stepwise flight paths of the Learjet 25, the measurements of ice crystals were sorted into 0.5 km vertical layers. In **Paper I**, the layers were chosen based on the UND Citation altitude changes at-one minute temporal resolution.

Table 1: Measurement times and altitudes of the flight profiles studied in this thesis. Flight A and B are based on **Paper I** and C and D based on **Paper II**, where they are named as A and B. Time is given in UTC with the corresponding solar zenith angle,  $\theta$  [ $^\circ$ ].

	Flight A	Flight B	Flight C	Flight D
Date	13 March 2000	13 March 2000	23 March 2010	24 June 2010
Time [UTC]	18:42–18:55	21:50–22:16	16:58–17:56	14:35–15:58
$\theta$ [ $^\circ$ ]	39.18–39.34	59.1–63.7	36.5–42.1	42.7–52.3
Cloud altitude [km]	6.8–8.8	4.7–7.9	9.5–11.5	8.0–11.5

The composite size distribution of ice crystals used in **Paper I** was determined using a Forward Scattering Spectrometer Probe (FSSP), a one-dimensional cloud probe (1DC), and a two-dimensional cloud probe (2DC) in size ranges of  $D < 50 \mu\text{m}$ ,  $50 \mu\text{m} < D < 120 \mu\text{m}$  and  $D > 120 \mu\text{m}$ , respectively. In **Paper II** the composite size distributions were generated by SPEC and available on-line in ARM data archive (<http://www.archive.arm.gov/discovery/>). In these distributions, a Fast Forward Scattering Spectrometer Probe (FFSP) with an open path design was used to characterize particles with  $D < 50 \mu\text{m}$ , a Two-dimensional Stereo probe (2DS) for  $50 \mu\text{m} < D < 1200 \mu\text{m}$ , and a 2-D precipitation Probe (2DP) or a High Volume Precipitation Sampler (HVPS-3) for particles larger than  $D > 1200 \mu\text{m}$ . Since the size of small ice crystals could not be reliably determined from the in situ measurement as a result of possible shattering effects (Korolev et al., 2011, 2013), the measured concentration of small ice crystals was treated as an upper bound for the concentration.

In **Paper I**, four different techniques for computing mass from the 2DC size distributions were compared against a mass content that was directly measured by a Counter-flow Virtual Impactor (CVI). These techniques were based on different assumptions on how mass varies depending on the maximum dimensions and area ratios of ice crystals. Out of these techniques, the one using a size-shape distribution of crystals based on 2DC and CPI measurements was found to provide a mass estimate most consistent with CVI data. Hence in **Paper I**, as also in **Paper II**, the size-dependent shape distributions of large ice crystals were based on the CPI images measured in situ. In **Paper I**, CPI was used to characterized crystals with  $D > 120 \mu\text{m}$  whereas in **Paper II**, crystals with  $D > 100 \mu\text{m}$ . The Automated habit classification algorithm by Um and McFarquhar (2009) and the automatic ice-cloud particle habit classifier, IC-PCA, by Lindqvist et al. (2012) were used to determine the fraction of different habits as a function of particle size from the CPI images in **Papers I** and **II**, respectively. The former algorithm sorts the crystals automatically into seven classes (column, plate, bullet rosette, budding bullet rosette, small and large irregular, and spherical) and the

Table 2: The final habit classes of large ice crystals that were created by combining CPI-based habit classes and further interpreted as Yang et al. (2000) habits in **Paper I** and as Yang et al. (2013) habits with three different roughness options in **Paper II**.

Label	habits of Yang et al. (2000)	habit classes of Um and McFarquhar (2009)
COL	solid column	column
ROS	4-branch bullet rosette	bullet rosette
BUD	6-branch bullet rosette	budding bullet rosette
PLA	plate	plate
SPH	rough aggregate	spherical
SIR	rough aggregate	small irregular
BIR	rough aggregate	big irregular
habit class	habits of Yang et al. (2013)	habit classes of IC-PCA
column	hollow column	columns and bullets
column agg	8-element column aggregate	column aggregates+bullet rosette aggregates
bullet rosette	bullet rosette	bullet rosettes
plate	plate	plate
plate agg	5-elementplate aggregate	plate aggregate
irregular	10-element plate aggregate	irregular

latter into 8 classes (bullet, column, column aggregate, bullet rosette, bullet rosette aggregates, plate, plate aggregate, and irregular). These observed habit classes and the habit classes of the optical property databases are listed in Table 2. Because the database of Yang et al. (2013) does not cover all the IC-PCA habit classes, we chose to classify bullets as columns and bullet rosette aggregates as column aggregates. Due to the lack of reliable in situ measurements of the shapes of small ice crystals, their shape was considered to be unknown. In **Paper I**, three alternative shapes models were considered for crystals with  $D < 120 \mu\text{m}$ : Gaussian random spheres, grs, (Noussainen and McFarquhar, 2004), droxtals (Yang et al., 2003), and Chebyshev particles (McFarquhar et al., 2002). These shape models were used to assess the impact of shape of small ice crystals on radiation. As newer investigations have revealed that the assumption of small ice crystals being quasi-spherical may be due to instrument limitations (Um and McFarquhar, 2011), in **Paper II**, all crystals with  $D < 100 \mu\text{m}$  were assumed to be hollow columns. As the concentrations of small ice crystals are also largely uncertain, alternative representations were used to characterize the number distributions functions,  $n(D)$ , for small ice crystals. In **Paper I**, three and in **Paper II**, four alternative  $n(D)$  were used to test the sensitivity of the simulated radiances to these concentrations. The used size-shape distributions based on different assumptions about small ice crystals are described in Table 3. In addition to the measurement-based shape distributions of large ice crystals (*large*), idealized single-habit distributions of crystals with  $D > 120 \mu\text{m}$  were used in **Paper II**.

In both **Papers I** and **II**, the size-shape distributions were combined with the single-scattering properties obtained from the state-of-the art databases described in Section 5.1. For the single-habit distributions the size distribution were combined with the single scattering properties of that habit and then integrated over the size distribution to obtain the vertical profiles of ensemble-averaged optical properties. For the CPI based habit distributions, the optical properties of each habit were weighted by the habit fractions before size integration. In both cases, Equations 12–17 introduced in Section 3.1 were used. **Paper I** investigates wavelengths from 300 to 2800 nm with 17 bands and **Paper II** a monochromatic radiation at  $\lambda = 670 \text{ nm}$ .

Table 3: The size-shape distributions of ice crystals. Note that the value of maximum dimension  $D$  used to divide crystals into small and large crystals is different in **Papers I** ( $D = 120 \mu\text{m}$ ) and **II** ( $D = 100 \mu\text{m}$ ). The concentration,  $n(D)$ , of large ice crystals was always based on the in-situ measurements, but was varied for small ice crystals.

Label	Large crystals	Small crystals
$large_{A/B}$	CPI based	-
large+droxtal	CPI based	droxtals with $n(D < 120\mu\text{m})$
large+Chebyshev	CPI based	Chebyshev with $n(D < 120\mu\text{m})$
large+grs	CPI based	grs with $n(D < 120\mu\text{m})$
large+grs50	CPI based	grs with $n(50 < D < 120\mu\text{m})$
$large_{C/D}$	CPI based	-
large+ $small_{50}$	CPI based	hollow columns with 50% of $n(D < 100 \mu\text{m})$
large+ $small_{100}$	CPI based	hollow columns with 100% of $n(D < 100 \mu\text{m})$
large+ $small_{200}$	CPI based	hollow columns with 200% of $n(D < 100 \mu\text{m})$

### 6.1.2 Mineral dust

In **Papers III** and **IV**, the optical properties of mineral dust were obtained by using spherical and spheroidal model particles. The radiative effects of nonsphericity of dust were investigated using spheroidal shape distributions suggested by Merikallio et al. (2011). It is noted, that these shape distributions were not used to resemble the aspect ratio distribution of natural dust particles, but to mimic their scattering properties. When non-spherical model particles are used instead of spheres to compute the optical properties, the measure of size (size-equivalence) needs to be established. In **Paper III**, the importance and impact of size equivalence on modeled radiative fluxes was quantified by using two different approaches: mass-conserving and  $\tau$ -conserving cases. In the mass-conserving case, all spherical particles were replaced with nonspherical particles with the same mass. In the  $\tau$ -conserving case, the number concentration of spheroids was modified so that the optical thickness at a reference wavelength  $\lambda = 545 \text{ nm}$  was the same for spherical and spheroidal dust particles. Strictly speaking, in this  $\tau$ -conserving case, the optical thicknesses for spheres and spheroids coincide only at the reference wavelength (achieving the same  $\tau$  at all wavelengths would have required, unrealistically, a wavelength-dependent number concentration of spheroids!). Obviously, the optical thickness of spheroidal dust is different in the mass-conserving and

$\tau$ -conserving cases. In **Paper IV**, the mass-equivalence (named volume-equivalence in **Paper IV**) was considered the most reasonable definition of nonsphericity effect in a climate-aerosol model that predicts both the number concentration and the mass of the particles. However, in some cases, e.g., when the optical thickness is available from remote sensing data, it is more meaningful to conserve the optical thickness rather than the total mass. Thus, in **Paper III** the  $\tau$ -conserving case was also considered.

The spheroidal shape distributions used in this thesis included ensembles of aspect ratios with the shape parameter  $\xi$  varying from -1.8 to 1.8 with an increment of 0.2. This resulted in 19 shapes: nine oblates, a sphere, and nine prolates. In **Paper III**, three shape distributions were considered: one consisted solely of spheres ( $\xi = 0$ ), and the other two included spheroids with either equal weights (hereafter, the  $n = 0$  distribution) or with larger weights to the oblates and prolates that deviate most from the sphere (hereafter, the  $n = 3$  distribution). The latter, considered also in **Paper IV**, is suggested by Merikallio et al. (2011) to be used in climate modeling. Of all the spheroidal shape distributions studied by Merikallio et al. (2011), the  $n = 3$  distribution gave the overall best representation of the asymmetry parameter of mineral dust. It is emphasized that the spherical and spheroidal distributions were used in this thesis to obtain the dust optical properties and not to imply that these distributions would describe the aspect ratio distribution of real dust particles.

The size distributions of mineral dust were assumed to be log-normal. In **Paper III**, 13 size distributions with a geometric standard deviation of  $\sigma_g = 2.0$  were investigated. The alternative size distributions covered particle radii from 0.1 to 19  $\mu\text{m}$  with the effective radius varying from 1.0 to 4.0  $\mu\text{m}$ . From the distributions,  $r_{\text{eff}} = 1.5 \mu\text{m}$  was chosen to represent a background dust case and  $r_{\text{eff}} = 4.0 \mu\text{m}$  a dust storm case. In **Paper IV**, the log-normal size distributions of both accumulation ( $\sigma_g = 1.59$ ) and coarse modes ( $\sigma_g = 2.0$ ) of ECHAM5.5-HAM2 were used. The size distribution of the spheroids was derived from the aerosol mass and number concentration simulated by HAM2, similar to the default treatment of spheres in HAM2. Thus, mass-equivalence was assumed in the conversion between sphere and spheroid size. However, spheroids were also compared against volume-to-area ( $V/A$ ) equivalent spheres. These were implemented so that each original sphere with radius  $r$  needed to be replaced with 1.5364 spheres with radius  $r' = 0.86663r$ . In practice, this treatment approximately eliminates the differences in  $\tau$  between spheres and spheroids.

The optical properties for the used size-shape distributions of spheroids were obtained from the database of Dubovik et al. (2006). The refractive index of dust used in **Papers III** and **IV** was adapted from ECHAM5.5-HAM2 and it is based on the work by Sokolik and Toon (1999) and Kinne et al. (2003). In **Paper III**, 23 wavelength bands covering the range from 0.28 to 4  $\mu\text{m}$  were used. For the aerosol optics look-up tables (LUTs) created in **Paper IV**, the  $C_{\text{ext}}$ ,  $\lambda$  and  $g$  were represented as function of the refractive index ( $m$ ) and the size parameter ( $x$ ) separately for the two log-normal modes. While the impact of dust nonsphericity may be important also in the longwave region, the new LUTs of spheroidal dust were computed only to cover the shortwave calculations, because the range of refractive index values in the database of Dubovik et al. (2006) is not sufficient to cover all of the longwave region. The LUTs using mass-equivalent spheroidal shape distributions are formed similarly as the original LUTs of ECHAM5.5-HAM2 to minimize the need for changes. The original LUTs were also recomputed with both the Mie code and the spheroid optics database of Dubovik et al. (2006) using only  $\xi = 0$  (a sphere) to ensure that they are indeed generated correctly. The very minor differences observed convinced us that the differences between LUTs of spheres and spheroids correctly represent the shape effect rather than any artifacts in the numerical computations.

## 6.2 Examples of the ensemble-averaged optical properties

The single-scattering properties (and ensemble-averaged optical properties) of both ice crystals and dust particles depend on the assumed size-shape distributions, and therefore, the comparison of optical properties of ice vs. dust is necessarily somewhat ambiguous. That said, a few basic differences in the optical properties of ice and dust are now introduced, based on the size-shape distributions and refractive indexes used in this thesis. Examples of the vertically integrated, wavelength-dependent  $g$ ,  $\omega$ ,  $K_{\text{ext}}$  of an ice cloud are shown in Figure 6, based on the five size-shape distributions of ice crystals of flights A and B. Furthermore, the dependence of  $\tau$ ,  $\omega$  and  $g$  of spherical dust particles on both wavelength of the radiation and the effective radius of spherical dust particles are shown in Figure 8. Regarding the wavelength dependence, the following can be noted:

- In the ice cloud case, the volume-extinction coefficient  $K_{\text{ext}}$  is almost spectrally flat in the SW region. This is because most ice crystals are much larger than the

wavelength and thus  $Q_{\text{ext}} \approx 2$ , almost independent of wavelength. In the dust case,  $\tau$  (and also  $K_{\text{ext}}$ ) are slightly larger in the near-IR region than in the visible region, the wavelength of maximum  $\tau$  being roughly equal to  $r_{\text{eff}}$ .

- The wavelength dependence of single-scattering albedo is strikingly different for ice clouds than dust. The absorption by ice is very weak ( $\omega \approx 1$ ) up to a wavelength of  $\lambda \approx 1 \mu\text{m}$  but increases at larger wavelengths,  $\omega$  reaching  $\approx 0.75$  at  $\lambda \approx 2.1 \mu\text{m}$ . In contrast, for dust, absorption is strongest in the UV region, with values of  $\omega$  as low as  $\approx 0.6$ . In most of the visible and near-IR region,  $\omega \approx 0.90 - 0.99$  for dust. The different spectral dependencies of single-scattering albedo are related to the imaginary part of the refractive index, which is largest for dust in the UV region but for ice in the near-IR region.
- The spectral dependence of asymmetry parameter is also different for ice clouds and dust. In the ice cloud case,  $g \approx 0.75 - 0.80$  in the visible region but increases to values up to  $\approx 0.9$  in the near-IR region. For dust, asymmetry parameter is largest in the UV region, where the value is  $\approx 0.9$ , while in most of the visible and near-IR regions  $g \approx 0.65 - 0.75$ .

Next it is discussed how the use of alternative size-shape distributions affects the ensemble-averaged optical properties of ice and dust and how these effects depend on the wavelength. First, it is noted from Figure 6 that particles in the size range from 50 to 120  $\mu\text{m}$  do not contribute much to the optical properties of the ice cloud in these particular cases. Particles with  $D < 50 \mu\text{m}$ , however, can contribute significantly, and thus uncertainties in their concentrations impact optical properties depending on the shape model used to represent their shape. The largest values of  $g$  and  $\omega$  occur when using the Chebyshev assumption for the shape of the small particles, followed by the Gaussian random sphere, grs, and droxtal assumptions, which is consistent with the analyses by Um and McFarquhar (2011). Based on the cloud optical thickness (integrated over cloud depth), it is evident that small crystals can make significant contributions to the cloud optical thickness if their maximum possible concentrations are assumed. Depending on the shape assumption (Chebyshev, grs, or droxtal), this contribution was 17.6%–21.4% (13.3%–16.4%) of the optical thickness of ice crystals larger than 50  $\mu\text{m}$  in case A (case B).

Ice crystal phase functions play a key role in determining the angular distribution of disk and circumsolar radiances, as also noted in **Paper II**. Therefore, to aid the inter-

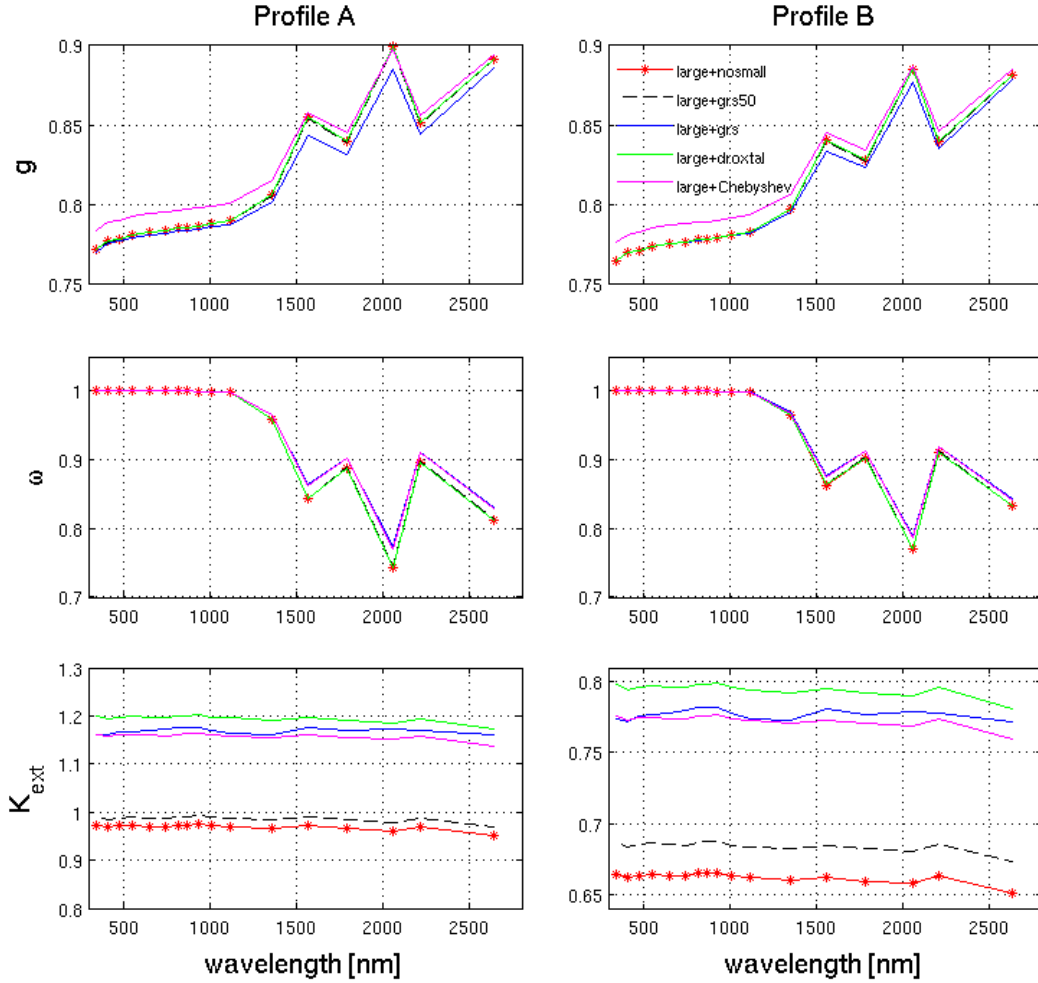


Figure 6: The wavelength dependence of the optical properties of ice cloud based on the different size-shape distributions of flight A and B. Values of vertically integrated ensemble-averaged asymmetry parameter,  $g$ , single-scattering albedo,  $\omega$ , and volume-extinction coefficient  $K_{\text{ext}}$  ( $\text{km}^{-1}$ ) are shown. Figure adapted from **Paper I**.

pretation of the angular distribution of radiances, the impact of ice crystal properties on the phase function (integrated over the cloud depth and the size-shape distribution) is shortly described. The general shape of  $P_{11}$  was similar for all in situ based size-shape distributions considered in **Paper II**, with values of  $P_{11}$  decreasing by roughly four orders of magnitude from the exact forward direction  $\gamma = 0^\circ$  to  $\gamma = 10^\circ$  for flight C and by nearly five orders of magnitude for flight D. The slope was steeper for flight D than C due to the presence of larger ice crystals in the flight D. For larger ice crys-

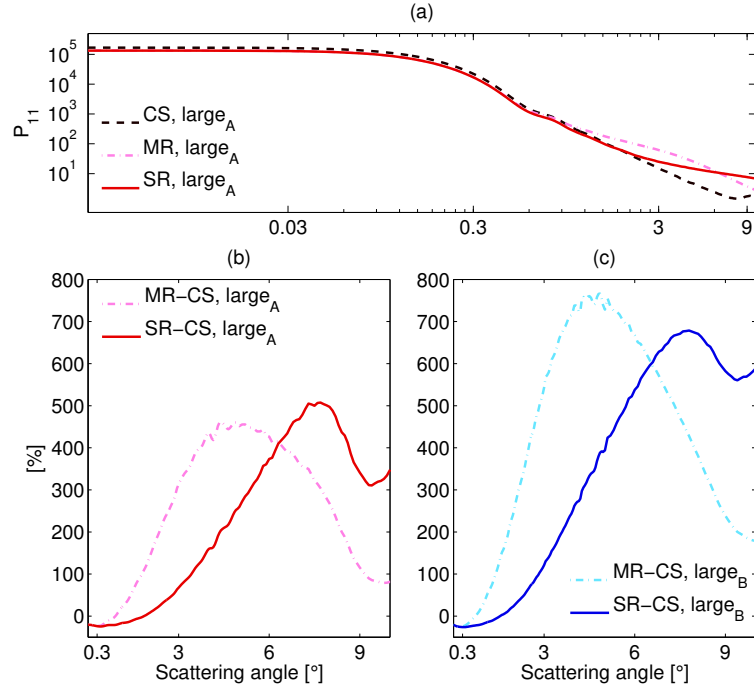


Figure 7: Sensitivity of the phase functions of ice clouds to the roughness of large ice crystals. **(a)** The  $P_{11}$  of the in-situ-based size-shape distribution of smooth, moderately and severely rough ice crystals of flight C ( $large_C$ ). **(b)** and **(c)** The relative differences in  $P_{11}$  between MR and CS ice crystals and between SR and CS ice crystals of flights C and D. Figure adapted from **Paper II**.

tals the diffraction peak is sharper and narrower, so that the phase function increases at very-near forward directions but decreases at larger scattering angles up to a few degrees. The differences in phase function related to ice crystal habit were relatively subtle compared to the large angular slope of  $P_{11}$  in near-forward directions, but not negligible. It was also found that the impact of the habit depends somewhat on the assumed ice crystal roughness. Figure 7a compares  $P_{11}$  corresponding to the three roughness assumptions (smooth and moderately and severely rough) for the  $large_C$  size-shape distributions, while Figure 7b–c show the relative differences between MR and SR ice crystals and the completely smooth ice crystals for the  $large_C$  and  $large_D$  distributions. Quantitatively, the impact of roughness is very large and clearly exceeds that of ice crystal habit. The  $P_{11}$  for rough ice crystals is lower than for smooth crystals in very-near-forward directions, but larger at larger angles. Furthermore, the phase function for moderately rough crystals exceeds that for severely rough crystals up to

around  $6^\circ$  but at larger angles, severely rough crystals yield the largest phase function. The relative differences between MR and CS crystals peak at smaller scattering angles ( $4^\circ - 5^\circ$ ) than the differences between SR and CS crystals ( $7^\circ - 8^\circ$ ). These differences are mainly related to rays that are transmitted through ice crystals, entering and exiting through parallel crystals faces, and how roughness is treated by distortion of surface slopes in the database of Yang et al. (2013).

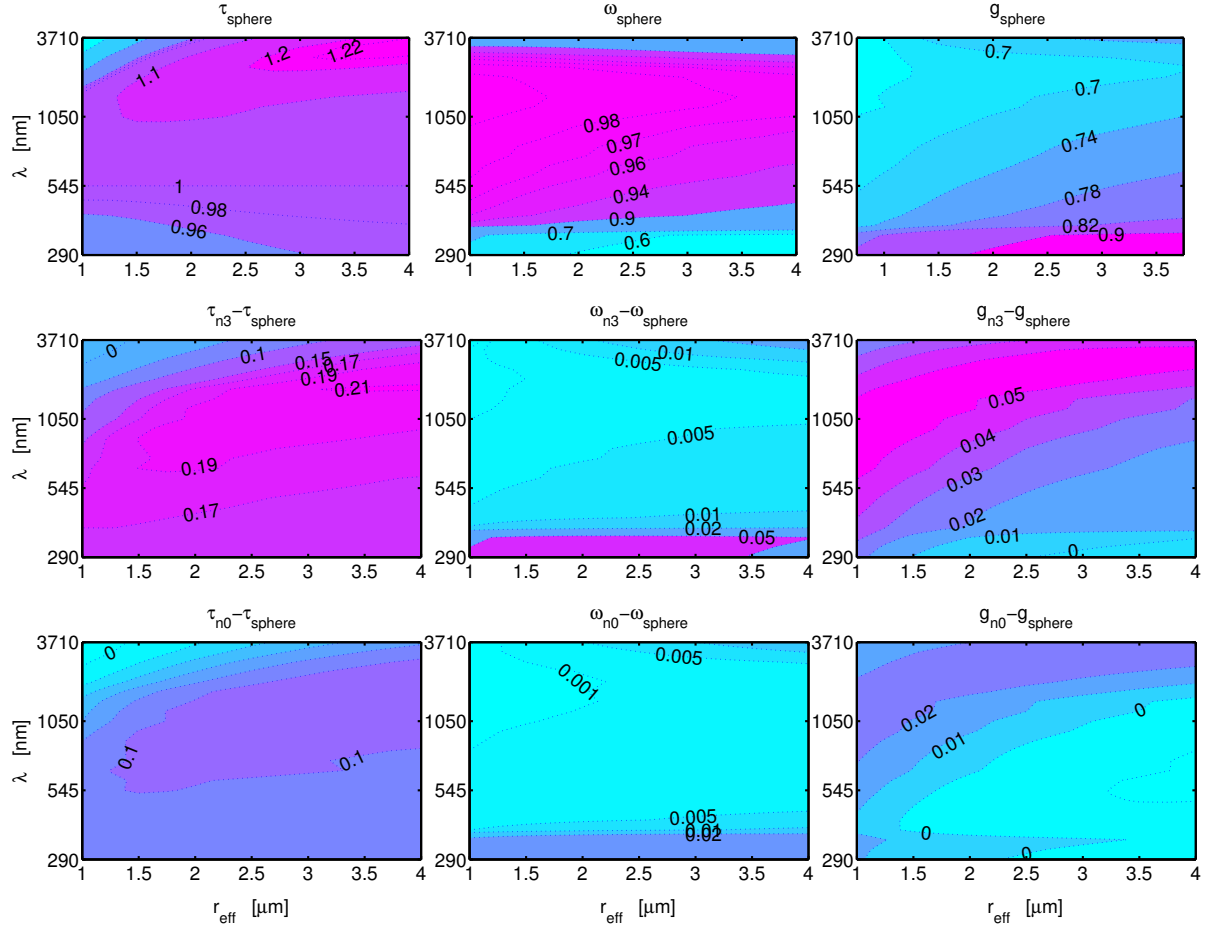


Figure 8: Top row: The optical thickness ( $\tau$ ,  $\tau_{\text{sphere}}(545) = 1$ ), single-scattering albedo ( $\omega$ ), and asymmetry parameter ( $g$ ) for spherical dust particles. Middle and bottom row: The differences in  $\tau$ ,  $\omega$  and  $g$  between the  $n = 3$  distribution of spheroids and spheres and between the  $n = 0$  distribution of spheroids and spheres, respectively. Results are shown as a function of wavelength ( $\lambda$ ) and size distribution (effective radius,  $r_{\text{eff}}$ ). For spheroids, the mass-conserving case is adopted. Figure adapted from **Paper III**.

The optical properties of size-shape distributions of dust are shown in Figure 8 as a function of  $\lambda$  and  $r_{\text{eff}}$ . Both the decrease in single-scattering albedo and the increase in asymmetry parameter with increasing  $r_{\text{eff}}$  are expected effects of increasing particle size. Note that here the optical thickness of spheres is fixed to unity at the 545 nm wavelength ( $\tau_{\text{sphere}}(545 \text{ nm}) = 1$ ). For mass-conserving spheroids, the optical thickness varies solely according to their respective  $C_{\text{ext}}$  values, being nearly always larger than that for spheres (by up to 19%). The differences are positive because for a given particle mass, the surface area is larger for spheroids than spheres. From Figure 8 it is seen that spheres and the two shape distributions of spheroids produce very similar single-scattering albedos. The absorption of dust is only slightly reduced when spheroidal model particles are used instead of spherical ones. This agrees well with earlier studies based on spheroids Mishchenko et al. (1997); Kahnert et al. (2007). The asymmetry parameter of the  $n = 3$  distribution tends to be larger than for spheres (by up to 0.05), whereas asymmetry parameter of the  $n = 0$  distribution can be either larger or smaller than for spheres. Overall, in **Paper III** it was concluded that the optical properties of the  $n = 3$  distribution deviate more from those of spherical particles than those based on the  $n = 0$  distribution. In Figure 1 of **Paper IV**, a case representative of dust microphysical properties in the ECHAM5.5-HAM2 aerosol-climate model was considered: dust particles in the insoluble coarse mode with an effective radius of  $r_{\text{eff}} = 1.2 \mu\text{m}$ . Mass-equivalent shape distributions of spheres and the  $n = 3$  distribution of spheroids were compared. In that case the dust optical thickness was larger for spheroids than for spheres almost throughout the SW region, with the largest differences (17–18%) in the UV and visible regions. Furthermore,  $g$  was higher for spheroids than spheres, by 0.03–0.05 at most wavelengths, which implies less backward scattering. The use of V/A-equivalent spheres instead of mass-equivalent ones reduces greatly the difference from spheroids for both optical thickness and single-scattering albedo (consistent with earlier studies by Grenfell et al. (1999); Neshyba et al. (2003), but the differences in  $g$  are rather increased slightly.

## 7 Results

### 7.1 Shortwave radiation in the presence of ice clouds

Figure 9 illustrates how the solar radiative effects of atmospheric ice crystals are investigated in this thesis. In **Paper I**, the shortwave radiative fluxes in the presence of an ice cloud were modeled with LibRadtran using airborne measurements of size-shape distributions of ice crystals combined with ice-crystal optical properties databases. In **Paper II**, the angular dependence of monochromatic disk and circumsolar radiances was simulated with MC-UniK. Again, the size-shape distributions of ice crystals were obtained in situ and combined with a database of optical properties of ice crystals. In both papers, radars, soundings and/or other ground-based measurements obtained at the SGP site were used to describe the vertical profile of the atmosphere in addition to the ice cloud. In both papers, the ground-based radiation measurements from the SGP site were used as a reference for the radiative transfer simulations. In **Paper I**, the

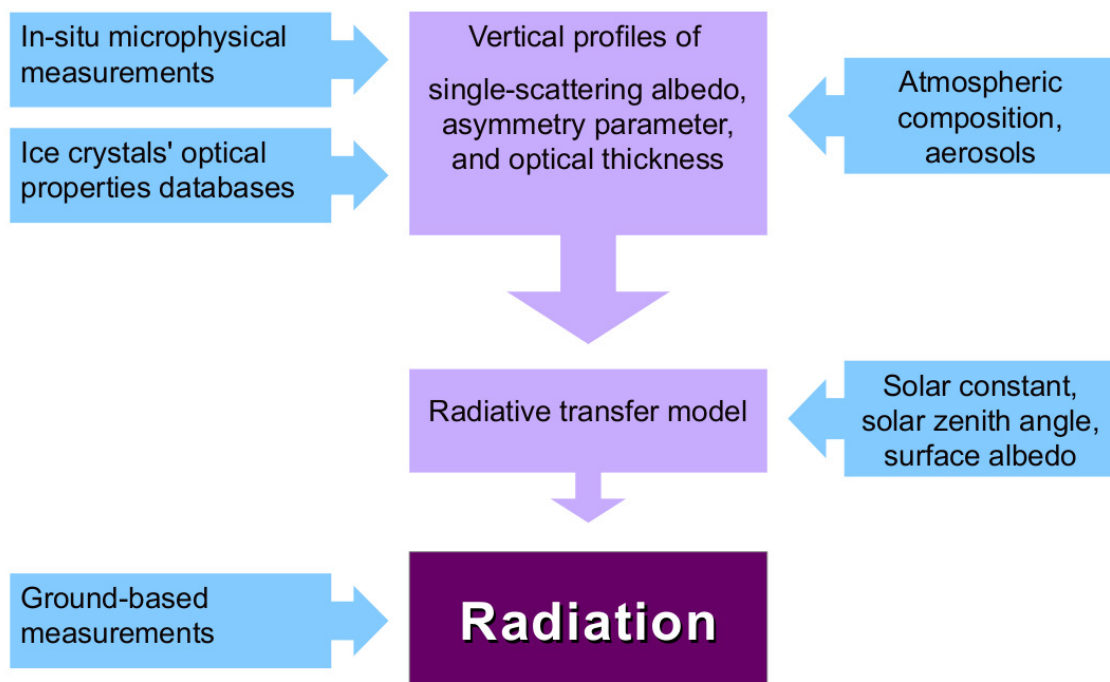


Figure 9: Schematic representation how the solar radiative effects of atmospheric ice crystals were investigated in this thesis.

shortwave radiation measurements were obtained from the best estimate flux value-added product Shi and Long (2002). This product automatically determined the best estimate of the direct and diffuse radiative fluxes ( $0.3 < \lambda < 2.8$  nm) from collocated instruments. In **Paper II**, the angular dependence of disk and circumsolar radiances were obtained from the Sun and Aureole Measurements (SAM) system at the 670 nm wavelength. SAM provides the disk and circumsolar radiances with a very high dynamic range and produces the disk and aureole radiances as a function of angle from the center of the Sun out to  $8^\circ$ .

### 7.1.1 Impact of small ice crystals on radiative fluxes

In **Paper I**, the impact of size and shape of ice crystals on simulated fluxes were investigated using five alternative size-distributions (Table 3). It was found that the concentration of small ice crystals can strongly influence the SW fluxes both at the surface and TOA. For example, the contribution of crystals with  $5 < D < 50$   $\mu\text{m}$  to the cloud radiative effect was stronger than that of crystals with  $50 < D < 120$   $\mu\text{m}$ . It was noted in that this most likely results from the artificial amplification of small crystals' concentrations due to the possible shattering on the tips of FSSP probe. The cloud radiative effect was also found sensitive to the shape of small ice crystals, Chebyshev particles yielding results deviating most from the other shape assumptions (droxtals and Gaussian random spheres). However, the use of the droxtal habit for small ice crystals produced the strongest cloud radiative effect at the surface, presumably due to their largest  $K_{\text{ext}}$  of all size-shape distributions.

### 7.1.2 Comparison of modeled and observed radiative fluxes

The simulated surface SW fluxes based on different size-shape distributions were also compared with ground-based measurements in **Paper I**. Before comparison, the amount of circumsolar radiation in the field of view of the instrument measuring direct radiation (i.e., within  $\approx 3^\circ$  from the center of Sun) needed to be quantified and added to the simulated direct flux. Similarly, the amount of circumsolar radiation lacking from the measured diffuse flux needed to be removed from the simulated diffuse flux. Based on the analysis presented in Appendix A of **Paper I**, this was done by performing the radiative transfer calculations twice for each case: first by using the actual

value of optical thickness (to derive the total flux), and second using optical thickness multiplied by 0.48 (to derive the apparent direct flux corresponding to the field of view of the measurements). All modeled fluxes discussed below include the correction.

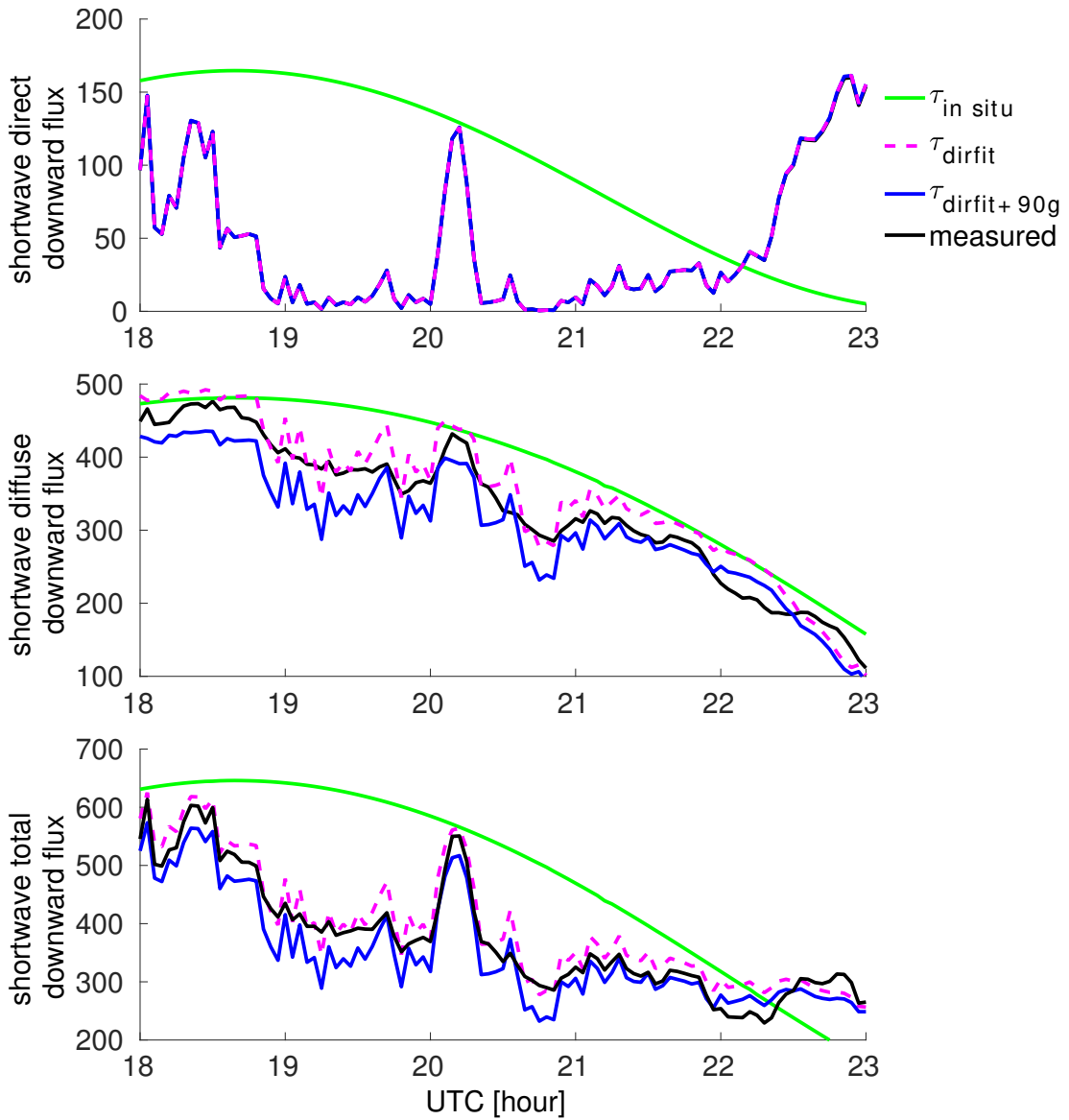


Figure 10: Shortwave direct, diffuse, and total downward fluxes [ $\text{Wm}^{-2}$ ] at the surface based on the sensitivity tests of **Paper I**. The simulations are also compared against ground-based measurements. Values of optical thickness of  $\tau_{in\ situ}$  are based on flight measurements; values of  $\tau_{dirfit}$  and  $\tau_{dirfit+90g}$  are retrieved from the direct radiation, and in the latter case,  $g$  is reduced by 10%.

It was found that the differences between the simulated and observed direct and diffuse fluxes were too large to be explained by uncertainties in the shape and concentrations of small ice crystals. Sensitivity tests suggested that the discrepancies occur because the real optical thickness was larger than that derived from the aircraft measurements most of the time. This might be due to the limited vertical and temporal coverage of the aircraft measurements. When the optical thickness was adjusted so that the measured and simulated direct fluxes matched ( $\tau_{\text{dirfit}}$ ), the modeled total downward flux agreed well with the measurements (mean difference less than  $19 \text{ Wm}^{-2}$ ). An example of the comparison of the measurements and radiative transfer simulations conducted using the optical properties ( $g$ ,  $\omega$  and  $\tau_{\text{in situ}}$  or  $\tau_{\text{dirfit}}$ ) of flight B is shown in Figure 10. It was suggested in **Paper I** that the remaining discrepancies between simulated and measured radiances could be partly due to the use of idealized ice crystals. It was shown that by slightly reducing asymmetry parameter (5–10%), the agreement with observations improved. A smaller asymmetry parameter could be associated to the presence of surface roughness or air bubble inclusions or other non-idealities in ice crystals. There is also observational evidence (Stephens et al., 1990; Kinne et al., 1992) that the ensemble-averaged asymmetry parameter for ice clouds may be as low as  $\approx 0.7$ , which is indeed about 10% smaller than the values obtained in **Paper I** for ideal ice crystals.

### 7.1.3 Impact of ice crystal properties on circumsolar radiance

In **Paper II**, the sensitivity of the simulated disk and circumsolar radiances to the size-shape distributions and roughness of ice crystals as well as to the ice-cloud and aerosol optical thicknesses ( $\tau_c$  and  $\tau_a$ ) was investigated. The radiances ( $\text{Wcm}^{-2}\mu\text{m}^{-1}\text{sr}^{-1}$ ) were simulated as a function of the angular distance from the center of the Sun ( $0^\circ$ ) out to  $8^\circ$  when looking towards the Sun from the ground. Figure 11 demonstrates the impact of aerosol and cloud optical thicknesses on the simulated disk and circumsolar radiances, for a solar zenith angle  $\theta = 40^\circ$ . For a pristine aerosol and cloud-free atmosphere (gases only), there is a huge contrast between the very strong radiances in the disk area and the weak and almost constant radiances in the circumsolar region. In the presence of background aerosols, the disk radiances are 10–20% smaller and the circumsolar radiances one to two orders of magnitude greater than in the gases only simulation. In the presence of a cirrus cloud, the circumsolar radiances are orders of magnitude greater than in the gases only and cloud-free cases, as seen from Figure 11.

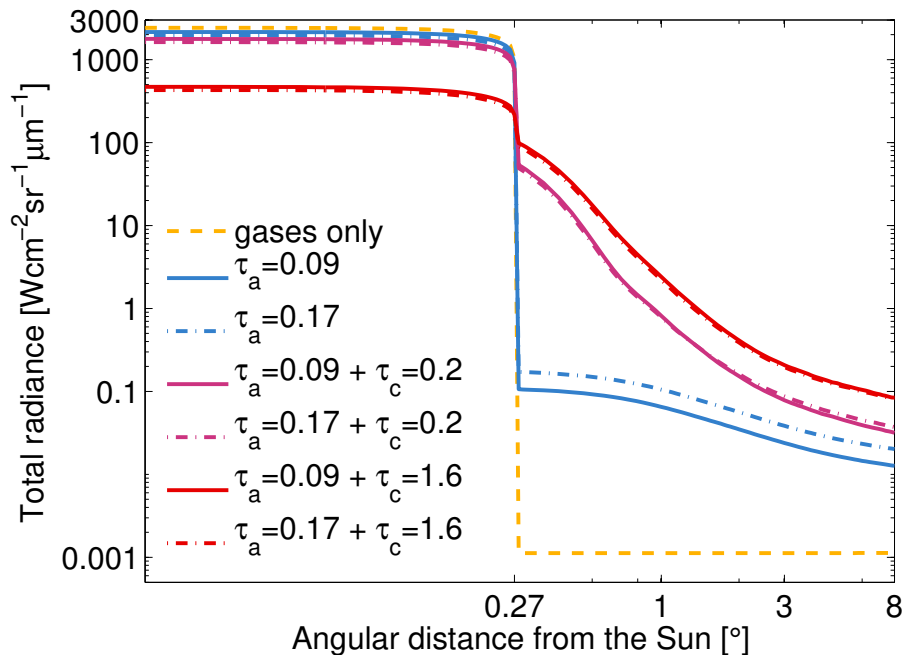


Figure 11: Impacts of the aerosol and cloud optical thicknesses ( $\tau_a$  and  $\tau_c$ ) on the simulated monochromatic radiances at  $\lambda = 670$  nm as a function of the angle from the center of the Sun out to  $8^\circ$ . Atmospheric and aerosol properties are based on flight C (flight A in **Paper II** with either  $\tau_a = 0.09$  or  $\tau_a = 0.166$ ). The cloud is described with the *large<sub>C</sub>* distribution of large severely rough ice crystals using two cloud optical thicknesses,  $\tau_c = 0.2$  and  $1.6$ . Data from **Paper II**.

The increase in diffuse radiance in the presence of an ice cloud is due to the strong forward-scattering peak of ice crystals, whereas the smaller disk radiances are due to the larger total optical thickness. The most striking effects, both in the absolute values and in the angular dependence, are seen in the angular region between the limb of the solar disk and  $1^\circ$ , where in the cloudy cases the radiances are between 100 and  $0.8 \text{ Wcm}^{-2} \mu\text{m}^{-1} \text{sr}^{-1}$  as compared with  $\sim 0.1 \text{ Wcm}^{-2} \mu\text{m}^{-1} \text{sr}^{-1}$  for the cloud-free cases. Changes in aerosol optical thickness also affect the absolute values of the radiances in the presence of an ice cloud, but not significantly their angular dependence.

In **Paper II**, it was found that the disk and circumsolar radiances depend substantially not only on  $\tau_c$ , but also on the ice crystal properties through their impact on the phase function. These findings are in line with previous studies by Reinhardt et al. (2014); Segal-Rosenheimer et al. (2013); DeVore et al. (2012). For a given cloud

optical thickness, the angular dependence of disk and circumsolar radiances was found to be most sensitive to assumptions about ice crystal roughness (or non-ideal features in general). Ice crystal sizes, concentrations and shapes were also found to play significant roles. The use of moderately or severely rough ice crystals instead of completely smooth crystals led to reduced radiances in the solar disk region while substantially increasing radiances in the circumsolar region at angles larger than  $\approx 2^\circ$ , with maximum differences as large as 400% between MR and CS crystals and 200% between SR and CS crystals. A larger portion of small ice crystals resulted in reduced disk radiances but increased radiances at angles of  $\approx 0.5^\circ - 5^\circ$ , with a maximum difference of up to  $\approx 100\%$  at  $\approx 1^\circ - 2^\circ$  from the center of the Sun, compared to the case with no small ice crystals. Column-like crystals (column, column agg and bullet rosette) tended to yield radiances with a steeper angular slope than plate-like (plate, plate agg and irregular) crystals, as they produced more diffuse radiance in the disk region and less in the circumsolar region than plate-like crystals. The relative differences between all single-habit distributions and the actually measured habit distributions were less than 10% in the disk region but up to 80% at angles larger than  $4^\circ$  from the center of the Sun.

#### 7.1.4 Comparison of modeled and observed circumsolar radiances

In **Paper II**, the simulated monochromatic radiances at  $\lambda = 670$  nm were compared with selected measurement times of SAM during both flights C and D. In the comparisons with SAM data, the ice-cloud optical thickness,  $\tau_c$ , was adjusted separately for each case based on the criterion that the simulated and SAM radiances averaged over the solar disk agreed within 3%. An example of the comparison of simulated and observed disk and circumsolar radiances at one measurement time during flights C and D is shown in Figure 12. The simulations shown were conducted both with and without the contribution of small ice crystals, assuming 100% of the measured small-crystal concentration in the former case. The values of  $\tau_c$  along with the solar zenith angle ( $\theta$ ) of the selected measurement times of SAM and the total apparent optical thicknesses (cloud+aerosols) retrieved from SAM are shown in Table 4. The derived values of  $\tau_c$  depend not only on the measurement time but also on the assumptions about ice crystal roughness and small ice crystals. In particular, it was found that larger cloud optical thickness was needed to match the observed radiances in the case of smooth than rough ice crystals. When neglecting the small ice crystals from the

Table 4: The values of solar zenith angle ( $\theta$ ) and optical thicknesses of cloud ( $\tau_c$ ), aerosol ( $\tau_a$ ) and gases ( $\tau_{gases}$ ) at  $\lambda = 670$  nm used in the comparison between simulations based on flights C and D and Sun and Aureole measurements (SAM) shown in Figure 12. The cloud was described with the size-shape distributions *large* and *large + small*<sub>100%</sub> of completely smooth (CS) and rough (MR and SR) ice crystals. Values of the fractional contribution of small ice crystals to cloud optical thickness for the *large+small*<sub>100%</sub> size-shape distribution ( $f_{small}$ ) and the total optical thickness (cloud+aerosols) retrieved from the SAM are also shown.

	Flight C	Flight D
$\theta$ [°]	38.3	50.0
$\tau_{SAM}$	1.0	1.0
$\tau_{gases}$	0.072	0.074
$\tau_a$	0.09	0.166
$\tau_c$ , CS, <i>large + small</i> <sub>100%</sub>	1.05	1.30
$\tau_c$ , MR or SR, <i>large + small</i> <sub>100%</sub>	1.00	1.15
$\tau_c$ , CS, <i>large + small</i> <sub>0%</sub>	1.25	1.45
$\tau_c$ , MR or SR, <i>large + small</i> <sub>0%</sub>	1.15	1.25
$f_{small}$ , <i>large + small</i> <sub>100%</sub>	79 %	27 %

size distribution, a larger value of  $\tau_c$  was needed to match the SAM disk radiances due to stronger forward scattering of large ice crystals. In addition, the derived values of cloud optical thickness tended to be larger than those reported by SAM. This is in line with DeVore et al. (2012) who found that the SAM-retrieved optical thickness needs to be corrected upward to account for forward scattering of ice crystals.

It was found that severely rough ice crystals mimicked the observed circumsolar radiances better than either the moderately rough or smooth crystals. This suggests that the severely rough crystals approximate better the phase function of ice crystals present during flights C and D. Moderately rough crystals overestimated the radiances at angles of a few degrees and the smooth crystals invariably underestimated the radiances at angles larger than  $\approx 3^\circ$ . The agreement tended to improve when crystals smaller than 100  $\mu\text{m}$  were neglected from the measured size distributions. This suggests that the measurements might have overestimated the concentrations of small crystals.

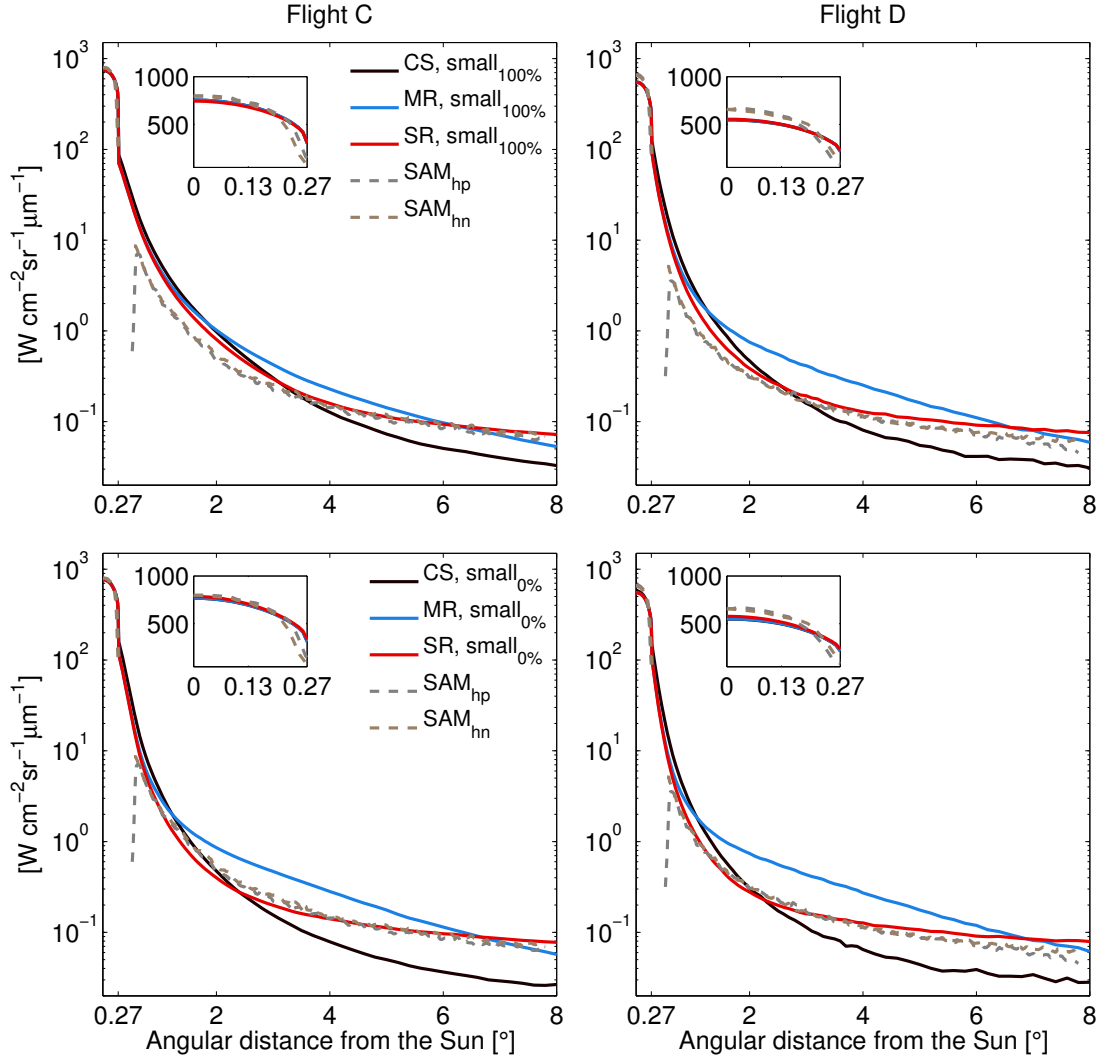


Figure 12: Comparison of the simulated monochromatic radiances at  $\lambda = 670$  nm and Sun and Aureole measurements (SAM) at one measurement time during both flights C and D. For the simulations the *large* distributions with 100% and 0% of measured concentrations of small ice crystals are used with optical thickness and solar zenith angles listed in Table 4. Smooth (CS) and rough (MR and SR) ice crystals are considered. Data from **Paper II**.

The results of **Paper II** suggest that it may well be possible to infer the particle roughness (or more generally, non-ideality) directly from the ground-based Sun and aureole measurements. In addition, the findings of **Paper II** add to the growing body of evidence (Cole et al., 2014; Ulanowski et al., 2014; Schmitt et al., 2016) suggesting that the scattering by natural ice crystals most often differs from their idealized counterparts, also in the near-forward directions (DeVore et al., 2012; Segal-Rosenheimer et al., 2013; Reinhardt et al., 2014).

## 7.2 Impact of dust particle nonsphericity on radiation

In **Papers III** and **IV** the local and global radiative effects of dust were investigated using optical properties of both spherical and spheroidal dust particles. Sensitivity of the results on different spheroidal shape distributions ( $n = 0$  and  $n = 3$ ) and size equivalences were investigated. The impact of assumed dust particle shape on the broadband direct shortwave radiative effects of dust (DRE) were investigated in paper **III** using LibRadtran. The impact of assumed dust particle shape on the simulated climate was tested in paper **IV** by employing the global aerosol-climate model ECHAM5.5-HAM2.

### 7.2.1 Local shortwave radiative impacts

Figure 13 illustrates how the shape impact of dust particles on SW fluxes were investigated in **Paper III**. Simulations were conducted using optical properties of either spheres, mass-equivalent spheroids (mass-conserving case), or (mass-equivalent) spheroids whose number concentration were modified so that they have the same mid-visible optical thickness ( $\tau(545 \text{ nm})$ ) as spheres ( $\tau$ -conserving case) (See Sect. 6.1.2). In addition, two alternative spheroidal shape distributions were investigated:  $n = 0$  and  $n = 3$  distributions. The radiative transfer simulations were conducted with LibRadtran using different size distributions and optical thicknesses of dust ( $r_{\text{eff}}, \tau$ ) over desert, grass and ocean surfaces with varying solar zenith angles ( $\theta$ ). The impact of the shape and size equivalence on diurnally averaged direct radiative effect of dust was investigated for both background dust and dust storm conditions using four representative  $\tau$  in the simulations. For spherical particles at the reference wavelength these were:  $\tau_{\text{sph}}(545) = 0.1/0.3/1.0/3.0$ . For other wavelengths and shape distributions, the optical thickness varied depending on  $C_{\text{ext}}$ . Altogether, for both shape distributions of

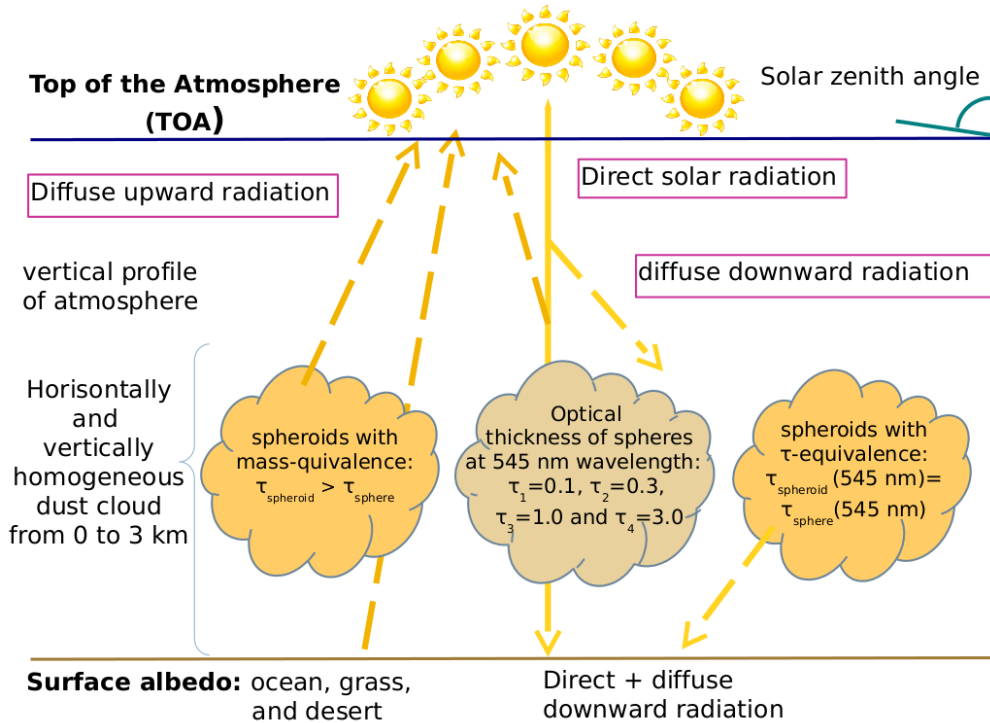


Figure 13: Schematic representation how the differences between solar radiative effects of spherical and spheroidal dust particles were investigated. Irradiances in the presence of five alternative dust clouds (with varying size distributions and optical thicknesses) were simulated with LibRadtran. Four of these dust clouds assumed optical properties based on spheroidal model particles (both mass- and  $\tau$ -conserving cases of  $n = 0$  and  $n = 3$  shape distributions).

spheroids ( $n = 0$  and  $n = 3$ ), eight alternative wavelength-dependent sets of optical properties were used. The shape impact was defined as the difference between direct radiative effects of dust based on spheroidal and spherical dust particles.

Based on the simulations conducted in **Paper III**, diurnally averaged direct radiative effects of dust both at the top of the atmosphere and at the surface tended to be negative. Often, the largest negative DREs were obtained over an ocean surface and the smallest over a desert surface, owing to the surface albedo being (on average) highest for desert and lowest for ocean. It was noticed that accounting for dust particles' nonsphericity can make the DRE either larger or smaller depending whether the  $n = 0$

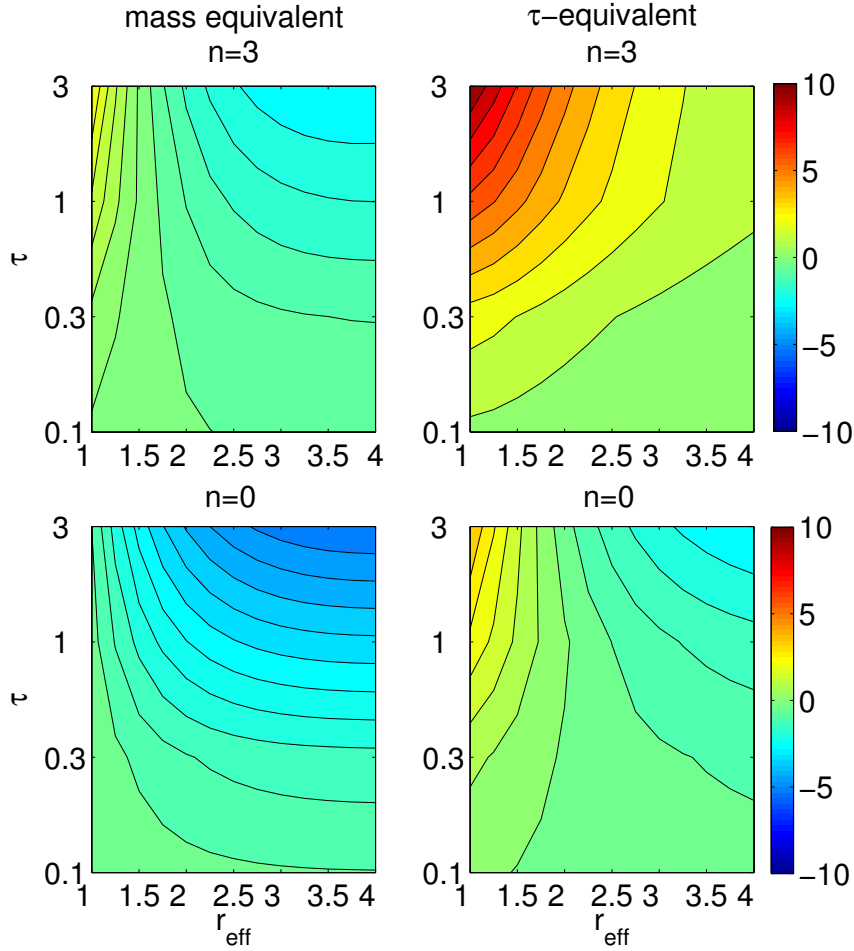


Figure 14: Difference between direct radiative effects of dust at the TOA ( $\text{Wm}^{-2}$ ) based on spheroidal ( $n = 0$  and  $n = 3$  distributions) and spherical dust particles (i.e., the shape impact) over ocean as a function of optical thickness ( $\tau$ ) and effective radius ( $r_{\text{eff}}$ ). Data from **Paper III**.

or  $n = 3$  distribution was assumed and whether the mass or optical thickness was conserved. These impacts depended on the values used for optical thickness, surface albedo and solar zenith angle. Figure 14 illustrates the dependencies of the shape impact on  $\tau$  and  $r_{\text{eff}}$  in the mass- and  $\tau$ -conserving cases. The shape impact is calculated here at the top of the atmosphere, assuming an ocean surface. As expected, in both the mass-conserving and  $\tau$ -conserving cases the largest shape impacts occur when the

dust optical thickness is large. In the mass-conserving case, the largest shape impacts occur when the dust particles are large, but in the  $\tau$ -conserving case when they are small. Furthermore, the sign of the shape impact can be different depending on the size equivalence and shape distribution of spheroids. The shape impacts were weaker for the mass-conserving cases (especially for the  $n = 3$  distribution) as a consequence of compensating nonsphericity effects of larger optical thickness and larger asymmetry parameter. When compared to spheres, in the mass-conserving case the  $n = 3$  shape distribution produces up to a 5% difference in DRE at the surface, but in the  $\tau$ -conserving case the difference could be up to 15%. Overall, the differences between mass- and  $\tau$ -conserving spheroids, those between the assumed shape distributions of spheroids and those between spheroids and spheres were roughly equal in magnitude. It was found that in some cases the DRE of dust using two different distributions of spheroids may deviate more from each other than either deviates from the DRE of spherical dust.

Overall, the findings of **Paper III** may be characterized as somewhat confusing: it turned out difficult to identify any simple pattern in the impact of particle shape on radiative effects. Even though a number of studies show that spheroids can mimic the scattering by real dust particles remarkable well, whereas spheres cannot, the results of **Paper III** suggested that the effects on radiative fluxes are moderate. Therefore, it was not clear whether the use of spheroidal particles instead of spheres would lead to significantly different results in climate simulations. This question was, however, deemed worth addressing explicitly, which was done in **Paper IV**.

### 7.2.2 Global climate impacts

**Paper IV** was continuation to the studies of SW direct radiative effects of dust nonsphericity reported in **Paper III** and, to our knowledge the first time that dust nonsphericity has been included in a global aerosol-climate model. (Shortly after, another climate modeling studies considering dust nonsphericity effects were published by Wang et al. (2013) and by Colarco et al. (2014)). In the aerosol-climate model, the impact of dust nonsphericity comes via the look-up tables (shortwave region only) of optical properties of dust in HAM2. The impact of nonsphericity was investigated by comparing results for the  $n = 3$  shape distribution of spheroids with both mass-equivalent and volume-to-area (V/A) equivalent spheres. For spheroids and mass-equivalent spheres

(the latter being the default treatment of dust optics in HAM2), the mass and number concentrations of particles were those predicted by HAM2. In the V/A case, the radius of spheres was multiplied by 0.86663 and their number concentration by 1.5364 as mentioned in Sect. 6.1.2. Actually, LUTs for the  $n = 0$  distribution were also generated but as the shape impacts on radiative fluxes were smaller than those with  $n = 3$ , the results were not discussed further.

Two experiments using the three optional LUTs (spheroids and mass- and V/A-equivalent spheres) were made in **Paper IV**. First, the impacts of the new dust optics on radiative fluxes were evaluated diagnostically. In this simulation, differences between the different shape options came directly from the differences in LUTs and not via any changes in the simulated meteorology. Thus, only the radiation calculations were made using the optional LUTs for insoluble dust and ECHAM5.5-HAM2 was integrated forward in time using only the mass-equivalent spheres. This model run lasted for 16 years from which the last 15 years were used for the analysis. Also in these simulations, the compensating nonsphericity effects on the dust optical thickness and asymmetry parameter were present in the mass-equivalent case, leading to small radiative flux differences. In this case, the SW direct radiative effects at the surface and TOA were slightly smaller (3–4%) for spheroidal than spherical dust particles. In contrast, in the V/A-equivalent case, the compensation was eliminated as optical thickness was almost the same for spheroids and spheres. Consequently, mainly due to the larger asymmetry parameter of spheroids, the direct radiative effect at the TOA (surface) was 20% (12%) smaller for spheroids than for spheres. These diagnostic analysis are in line with the small-to-moderate radiative effects of dust nonsphericity found in **Paper III**.

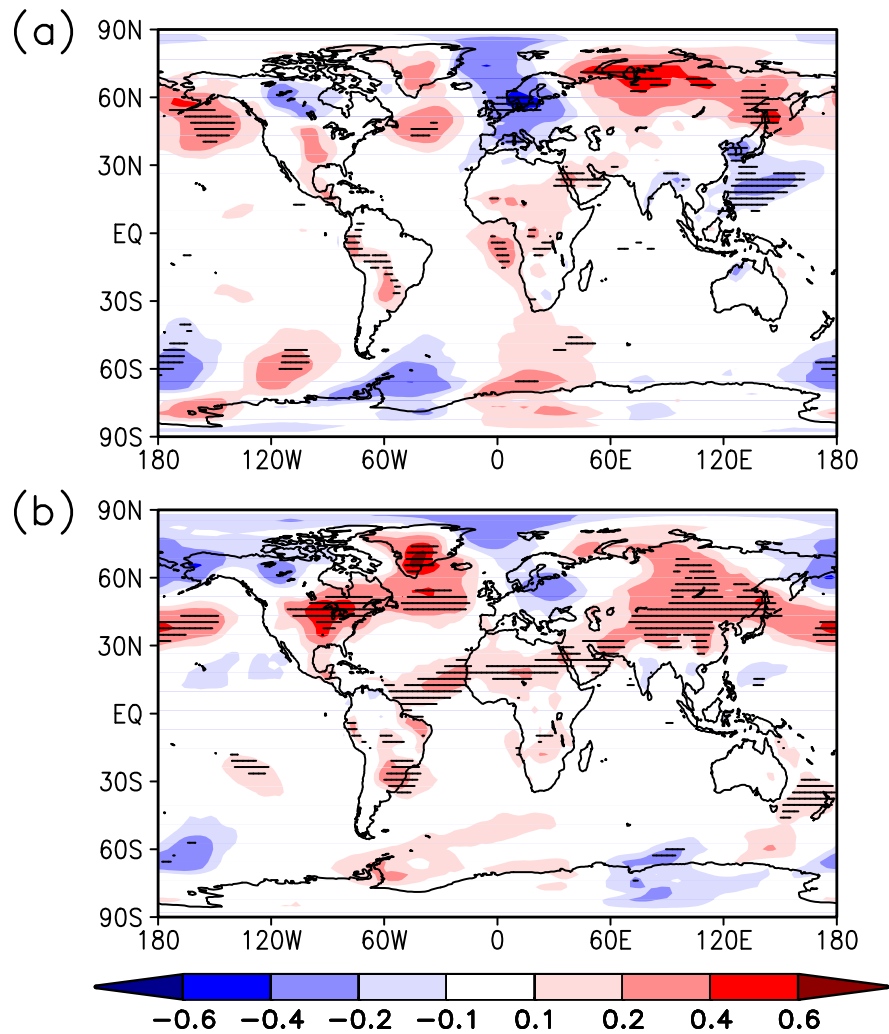


Figure 15: Difference in time-mean 2 m air temperature (K) in ECHAM5.5-HAM2 experiments (a) between spheroids ( $n = 3$ ) and mass-equivalent spheres (b) between spheroids ( $n = 3$ ) and V/A-equivalent spheres. Differences statistically significant at the 95% confidence level are marked with horizontal lines. The global mean difference is 0.03 K in (a) and 0.04 K in (b). Figure adopted from **Paper IV**.

In the second experiment, climate simulations were conducted with each of the LUTs. To reduce the impact of the model’s internal climate variability, rather intensive runs were made. For each three treatments of shape, two 50-year runs were conducted, from which the last 40 years were used in the analysis. From the climate simulations we analyzed the impact of dust nonsphericity on the distribution of (e.g.) temperature, sea-level pressure, precipitation and cloudiness. As an example, the impact of dust nonsphericity on simulated 2-m air temperature is shown in Figure 15, which is adopted from **Paper IV**. The statistical significance of the differences was evaluated following Räisänen et al. (2008). The largest local differences occurred at mid-to-high latitudes, with a maximum difference of 0.7 K between mass-equivalent spheroids and spheres in southern Greenland in the V/A-equivalent case. However, since there is no obvious physical reason for this feature, it is possible that it was caused by internal climate variability. One feature that probably represents a real physical signal is that, in the V/A-equivalent case, the spheroidal simulation was  $\approx 0.2$  K warmer than the spherical simulation in parts of the Sahara and the adjacent tropical Atlantic. This is what one would expect, considering that the dust DRE at the surface is smaller (i.e., less negative) for spheroids than spheres in the V/A-equivalent case. Overall, the effect of dust nonsphericity for climate simulations proved to be small and mostly indistinguishable from the model’s internal climate variability. This suggests that the impact of dust nonsphericity can be neglected in terrestrial climate modeling. There are presently other, much larger uncertainties in climate models than the treatment of optical properties of dust. For example, in **Paper IV** it was highlighted that the HAM2 model occasionally generated dust storms with unrealistically large aerosol optical depths.

## 8 Conclusions

Atmospheric ice crystals and mineral dust particles are important components in the local and global radiation balance through their role in the redistribution of radiative energy. The amount of solar radiation scattered and absorbed by these particles depends on their spatio-temporal single-scattering properties. Because these particles are not homogeneous spheres, but irregularly shaped there are challenges in establishing their single-scattering properties. The remaining large uncertainties in the ensemble averaged optical properties of ice and dust reflect uncertainties in their radiative effects. The solar radiative effects of ice and dust are studied in this thesis. The most important findings of this work are summarized below together with discussion of the limitations of the work and possible topics for future research.

This thesis demonstrated how SW irradiances and radiances in the presence of an ice cloud can be simulated based on the microphysical in situ measurements of atmospheric ice crystals. This is a unique way of connecting microphysical measurements via single-scattering properties to simulating radiation. This thesis expanded upon past studies examining cloud radiative interaction by clearly quantifying the distinct impact of uncertainties in the concentrations and shape of small ice crystals on irradiances and circumsolar radiances. It also offered interesting new insights into understanding the connection between particle morphology, cloud microphysics and cloud radiative effects. It was found that in the shortwave radiative transfer perspective, the size, shape, concentration and roughness of the ice crystals are important. The conclusions of this thesis add to the growing body of evidence that natural ice crystals tend not to be pristine, rather they appear to possess some deviation from the ideal ice crystals characteristic either in the form of surface roughness or air bubble inclusion or other non-idealities. This thesis, however, did not try to answer the question what these deviations might be. It was noted that to be able to mimic accurately the radiative fluxes and/or radiances in the presence of an ice cloud, more information about the size-shape distributions, concentrations, roughness and optical properties of ice crystals are still needed. In particular, there is large uncertainty in the measurements of small ice crystals' concentrations and shapes.

This thesis highlighted the importance of a consistent definition of "direct" solar radiation in measurements and modeling. The issue arises, because a typical instrument measuring the direct radiation has an opening angle of  $3 - 6^\circ$ , while the solar disk

has an opening angle of only  $0.53^\circ$  when observed from the ground. Besides direct radiation, the observed radiation can contain diffuse radiation originating from the disk and circumsolar region. Especially in the presence of an ice cloud, the amount of diffuse radiation in the observed "direct" radiation can be notable. If this is not properly accounted for in radiative transfer modeling, it can impact substantially the comparison of measured and modeled shortwave "direct" radiation. In addition, it can lead to biases in the retrieved cloud or aerosol properties. It was found in this thesis that the amount of circumsolar radiation in the instrument's field of view is sensitive especially to the roughness and size distribution of the ice crystals. The potential applications of these results include remote sensing of optical thickness, ice cloud properties based on the radiance field near the sun, the design of concentrating solar energy applications, and the development of ice cloud optical property parameterizations for weather and climate models.

This thesis also explored the impact of the nonsphericity of mineral dust particles, first in off-line radiative transfer simulations, and then in the first-ever climate model experiments using nonspherical dust optics. The nonspherical shape models employed in this work were composed of aspect ratio distributions of spheroids, the use of which in modeling the optical properties of mineral dust was carefully evaluated in the work by Merikallio et al. (2011). In the experiments with the ECHAM5.5-HAM2 model, the impact of dust nonsphericity proved to be small and mostly indistinguishable from the model's internal climate variability. Based on this, it was suggested that there is no need to replace the use of spherical dust model particles with spheroidal ones in aerosol-climate models. Clearly, in terrestrial climate modeling (and even in the modeling of atmospheric dust) there are presently other much larger uncertainties than the shape of dust particles. However, in contrast to its moderate effect on radiative fluxes, the effect of dust particle shape on the scattering matrix, including the phase function, is very strong and can cause errors in the retrieved optical thickness (Mishchenko et al., 2003). Thus, the use of spherical particles can cause errors in remote sensing and those applications may benefit from the use of spheroidal model particles instead of spherical model particles.

Like in almost any scientific work, there are simplifications and uncertainties in the present work that call for improvements in future studies. First, we are aware of several simplifications made in the ice cloud studies (**Papers I and II**) from which the cloud horizontal homogeneity and spatiotemporal collocation of the flight profiles and

the ground measurements are probably the most significant ones. In future studies these limitations could be alleviated by considering, in addition to in situ data, collocated radar and satellite data. This would allow the derivation of three-dimensional cloud fields and corresponding ensemble-averaged optical properties, from which surface irradiances and radiances could be calculated. Further, the simulated radiation could be compared against satellite and ground-based observations. This would not only improve the microphysical measurements, but also avoid problems associated with lack of collocation between microphysical and radiation measurements. Furthermore, the specification of three-dimensional cloud structure would support the use of three-dimensional (3D) radiative transfer models. In particular, our version of MC-UniK could be used for analyzing different cirrus cloud and aerosol scenarios and their 3D effects on near-forward radiances.

Further areas in need of improvement include the observations of the microphysical structure of non-spherical particles (both ice crystals and dust) and computation of their single-scattering properties. As noted above, substantial uncertainties remain in measuring the concentration and shapes of small ice crystals. Furthermore, while it has been demonstrated that scattering by natural ice crystals usually deviates from their idealized counterparts, the current ad-hoc treatments of ice-crystal nonideality in ice crystal optics databases are also subject to uncertainty. It is hoped that improved and more comprehensively validated descriptions of ice crystal single-scattering properties will become available in future databases. Finally, modeling the scattering by dust using spheroids may be considered another ad-hoc choice, whose range of validity is not fully known. In principle, an approach based on the actual measured shape of dust particles would be desirable. If specifications of dust optical properties based on such a first-principle approach become available in the future, it would be worth revisiting the questions of how dust particle shape impacts both remote sensing and climate simulations.

## References

- Anderson, G., Clough, S., Kneizys, F., Chetwynd, J., and Shettle, E. (1986). AFGL atmospheric constituent profiles (0-120 km). *Tech. Rep. AFGL-TR*, **86-0110**, Air Force Geophys. Lab., Hanscom Air Force Base, Bedford, Mass.
- Bailey, M., and Hallett, J. (2003). Nucleation effects on the habit of vapour grown ice crystals from  $-18^{\circ}$  to  $-42^{\circ}\text{C}$ . *Q. J. R. Meteorol. Soc.*, **128**, 1461–1483.
- Baran, A. J., and Francis, P. N. (2004). On the radiative properties of cirrus cloud at solar and thermal wavelengths: A test of model consistency using high-resolution airborne radiance. *Q. J. R. Meteorol. Soc.*, **130**, 763–778, doi:10.1256/qj.03.151.
- Baran, A. J. (2009). A review of the light scattering properties of cirrus. *J. Quant. Spectrosc. Radiat. Transfer*, **110**, 1239–1260, doi:10.1016/j.jqsrt.2009.02.026.
- Baran, A. J. (2012). From the single-scattering properties of ice crystals to climate prediction: a way forward. *Atmos. Res.*, **112**, 45–69.
- Barker, H, Goldstein, R., and Stevens, D. (2003). Monte Carlo simulation of solar reflectances for cloudy atmospheres. *J. Atmos. Sci.*, **60**, 1881–1894.
- Baum, B. A., Yang, P., Hu, Y.-X., and Feng, Q. (2010). The impact of ice particle roughness on the scattering phase matrix. *J. Quant. Spectrosc. Radiat. Transfer*, **111**, 2534–2549, doi:10.1016/j.jqsrt.2010.07.008.
- Baumgardner, D., and Korolev, A. V. (1997). Airspeed corrections for optical array probe sample volumes. *J. Atmos. Ocean. Tech.*, **14**, 1224–1229.
- Bohren C., F., and Huffman, D. R. (2007). Absorbtion and Scattering of Light by Small Particles. *Wiley-VCH Verlag GmbH*, New York, doi:10.1002/9783527618156.
- Boudala F. S, George, A. I., McFarlane, N. A., and Li, J. (2007). The Sensitivity of the Radiation Budget in a Climate Simulation to Neglecting the Effect of Small Ice Particles. *Journal of Climate*, **20**.
- Konoshonkin A., Wang, Z., Borovoi A., Kustova, N., Liu, D., and Xie, C. (2016). Backscatter by azimuthally oriented ice crystals of cirrus clouds. *Optics Express*, **24**(18).

- Borovoi, A. G., Burnashov., A., Cheng, A. Y. S. (2007). Light scattering by horizontally orientated ice crystals plates. *J. Quant. Spectrosc. Radiat. Transfer*, **106**(1), 11–20, doi:10.1016/j.jqsrt.2007.01.002
- Bryant, F. D. and Latimer, P. (1969) Optical efficiencies of large particles of arbitrary shape and orientation. *J. Colloid Interface Sci.*, **30**, 291–304.
- Buschmann, N., McFarquhar, G. M., and Heymsfield, A. J. (2002). Effects of observed horizontal inhomogeneities within cirrus clouds on solar radiative transfer. *J. Geophys. Res.*, **107**(D20), 4445, doi:10.1029/2001JD001273.
- Böhn-Vitense, E. (1989). Introduction to stellar astrophysics, Volume 2. *Stellar atmospheres*, Cambridge University Press.
- Bi, L., Yang, P., Kattawar, G. W., Baum, B. A., Hu, Y. X., Winker, D. M., Brock, R. S., and Lu, J. Q. (2009). Simulation of the color ratio associated with the backscattering of radiation by ice particles at the wavelengths of 0.532 and 1.064  $\mu$  m. *J. Geophys. Res.*, **114**, D00H08, doi:10.1029/2009JD011759.
- Cahalan, R. F., Oreopoulos, L., Marshak, A., Evans, K. F., Davis, A. B., Pincus, R., Yetzer, K. H., Mayer, B., Davies, R., Ackerman, T. P., Barker, H. W., Clothiaux, E. E., Ellingson, R. G., Garay, M. J., Kassianov, E., Kinne, S., Macke, A., O’Hirok, W., Partain, P. T., Prigarin, S. M., Rublev, A. N., Stephens, G. L., Szczap, F., Takara, E. E., Varnai, T., Wen, G., and Zhuravleva, T. B. (2005). The International Intercomparison of 3D Radiation Codes (I3RC): Bringing together the most advanced radiative transfer tools for cloudy atmospheres. *Bull. Amer. Meteor. Soc.*, **86**(9), 1275–1293.
- Claquin, T., Schulz, M., and Balkanski, Y. J. (1999). Modeling the mineralogy of atmospheric dust sources. *J. Geophys. Res.*, **104**(D18), 22243–22256, doi:10.1029/1999JD900416.
- Chen, G., Yang, P., Kattawar, G. W., Mishchenko, M. I. (2006). Scattering phase functions of horizontally oriented hexagonal ice crystals. *J. Quant. Spectrosc. Radiat. Transfer*, **100**, 91–102.
- Colarco, P. R., Nowottnick, E. P., Randles, C. A., Yi, B., Yang, P., Kim, K.-M., Smith, J. A., and Bardeen, C. G. (2014). Impact of radiatively interactive dust aerosols in the NASA GEOS-5 climate model: Sensitivity to dust particle shape and refractive index. *J. Geophys. Res.*, **119**, 753–786, doi:10.1002/2013JD020046.

- Cole, B. H., Yang, P., Baum, B. A., Riedi, J., and Labonnote, L. C. (2014). Ice particle habit and surface roughness derived from PARASOL polarization measurements. *Atmos. Chem. Phys.*, **14**, 3739–3750, doi:10.5194/acp-14-3739-2014.
- Chou, C., Formenti, P., Maille, M., Ausset, P., Helas, G., Harrison, M., and Osborne, S. (2008). Size distribution, shape, and composition of mineral dust aerosols collected during the African Monsoon Multidisciplinary Analysis Special Observation Period 0: Dust and Biomass-Burning Experiment field campaign in Niger, January 2006. *J. Geophys. Res.*, **113**, D00C10, doi:10.1029/2008JD009897.
- DeLand, M. T., Cebula, R., P., and Hilsenrath, E. (2004). Observations of solar spectral irradiance change during cycle 22 from NOAA-9 Solar Backscattered Ultraviolet Model 2 (SBUV/2). *J. Geophys. Res.*, **109**, D06304, doi:10.1029/2003JD004074.
- DeVore, J. G., Stair, A. T., LePage, A. J., Rall, D., Atkinson, J., Villanucci, D., Rappaport, S., Joss, P., and McClatchey, R. (2009). Retrieving properties of thin clouds from solar aureole measurements. *J. Atmos. Ocean. Techn.*, **26**(12), 2531–2548.
- DeVore, J. G., Stair, A. T., LePage, A. J., Rall, D., and Villanucci, D. (2012). Using scattering calculations to compare MODIS retrievals of thin cirrus optical properties with SAM solar disk and aureole radiance measurements. *J. Geophys. Res.*, **117**, D10204.
- Dubovik, O., Sinyuk, A., Lapyonok, T., Holben, B. N., Mishchenko, M., Yang, P., Eck, T. F., Volten, H., Muñoz, O., Veihelmann, B., van der Zande, W. J., Leon, J. -F., Sorokin, M., and Slutsker, I. (2006). Application of spheroid models to account for the aerosol particle nonsphericity in remote sensing of desert dust. *J. Geophysical Research*, **111**, D11208.
- Durant, A. J., Harrison, S. P., Watson, I. M., and Balkanski Y. (2009). Sensitivity of direct radiative forcing by mineral dust to particle characteristics. *Progress in Physical Geography*, **33**(1), pp. 80–102, doi:10.1177/0309133309105034.
- Ebert, E. E., and Curry, J. A. (1992). A parameterization of ice cloud optical properties for climate models. *J. Geophys. Res.*, **97**(D4), 3831–3836.
- Emde, C., Buras-Schnell, R., Kylling, A., Mayer, B., Gasteiger, J., Hamann, U., Kylling, J., Richter, B., Pause, C., Dowling, T., and Bugliaro, L. (2016). The li-

- bRadtran software package for radiative transfer calculations (version 2.0.1). *Geosci. Model Dev.*, **9**, 1647–1672, doi:10.5194/gmd-9-1647-2016.
- Feng, Q., Yang, P., Kattawar, G. W., Hsu, C. N., Tsay, S.-C., Laszlo, I. (2009). Effects of particle nonsphericity and radiation polarization on retrieving dust properties from MODIS observations. *J. Aerosol Sci.*, **40**, 776–789.
- Fouquart, Y., and Bonnel, B. (1980). Computations of solar heating of the Earth’s atmosphere: A new parameterization. *Beitr. Phys. Atmos.*, **53**, 35–62.
- Fridlind, A. M., Atlas, R., van Diedenhoven, B., Um, J., McFarquhar, G. M., Ackerman, A. S., Moyer, E. J., and Lawson, R. P. (2016). Derivation of physical and optical properties of midlatitude cirrus ice crystals for a size-resolved microphysics model. *Atmos. Chem. Phys.*, **16**, 7251–7283, doi:10.5194/acp-16-7251-2016.
- Fu, Q. (1996). An accurate parameterization of the solar radiative properties of cirrus clouds for climate models. *J. Clim.*, **9**, 2058–2282.
- Fu, Q., Yang, P., and Sun, W. B. (1998). An accurate parameterization of the infrared radiative properties of cirrus clouds for climate models. *J. Clim.*, **11**, 2223–2237, doi:10.1175/1520-0442(1998)011<2223:AAPOTI>2.0.CO;2.
- Gardiner, B. A., and Hallett, J. (1985). Degradation of in-cloud forward scattering probe measurements in the presence of ice particles. *J. Atmos. Ocean. Tech.*, **2**, 171–180.
- Green, S. F., and Jones, M. H. (2015). An Introduction to the Sun and Stars. *The Open University*.
- Grenfell, T. C., and Warren, S. G. (1999). Representation of a nonspherical ice particle by a collection of independent spheres for scattering and absorption of radiation. *J. Geophys. Res.*, **104**, 31697–31709.
- Hallett, J. (1976) Measurement of size, concentrations and structure of atmospheric particulates by the airborne continuous particle replicator. *Air Force Geophysics Laboratory Rep. AFGL-TR-76-0149*, Hanscom AFB, MA, 92 pp.
- Haywood, J., Francis, P., Osborne, S., Glew, M., Loeb, N., Highwood, E., Tanré, D., Myhre, G., Formenti, P., and Hirst, E. (2003). Radiative properties and direct radiative effect of Saharan dust measured by the C-130 aircraft during SHADE: 1. Solar spectrum. *J. Geophys. Res.*, **108**(D18), doi:10.1029/2002JD002687.

- Herbert, R. J., Murray, B. J., Dobbie, S. J., and Koop, T. (2015). Sensitivity of liquid clouds to homogenous freezing parameterizations. *Geophys. Res. Lett.*, **42**, 1599–1605, doi:10.1002/2014GL062729
- Hoose, C. and Möhler, O. (2012) Heterogeneous ice nucleation on atmospheric aerosols: a review of results from laboratory experiments. *Atmos. Chem. Phys.*, **12**, 9817–9854, doi:10.5194/acp-12-9817-2012.
- Heymsfield, A. J., Lewis, S., Bansemer, A., Iaquinta, J., Miloshevich, L. M., Kajikawa, M., Twohy, C., and Poellot, M. R. (2002). A general approach for deriving the properties of cirrus and stratiform ice cloud particles. *J. Atmos. Sci.*, **59**, 3–29.
- Jakson, J. D. (1999). Classical electrodynamics (3rd Ed.). *John Wiley & Sons, Inc.*, New York.
- Kahnert, M., and Kylling, A. (2004). Radiance and flux simulations for mineral dust aerosols: Assessing the error due to using spherical or spheroidal model particles. *J. Geophys. Res.*, **109**, D09203, doi:10.1029/2003JD004318.
- Kahnert, M. (2004). Reproducing the optical properties of fine desert dust aerosols using ensembles of simple model particles. *J. Quant. Spectrosc. Radiat. Transfer*, **85**, 3–4, 231–249, doi:10.1016/S0022-4073(03)00227-9.
- Kahnert, M., Nousiainen, T. and Räisänen, P. (2007). Mie simulations as an error source in mineral aerosol radiative forcing calculations. *Q. J. R. Meteorol. Soc.*, **133**, 99–307, doi:10.1002/qj.40.
- Kandler, K., (2009) Size distribution, mass concentrations, chemical and mineralogical composition, and derived optical parameters of the boundary layer at Tinfou, Morocco, during SAMUM 2006. *Tellus Ser. B*, **61**, 32–50.
- Kato, S., Ackerman, T. P., Mather, J. H., and Clothiaux, E. (1999). The k-distribution method and correlated-k approximation for a shortwave radiative transfer model. *J. Quant. Spectrosc. Radiat. Transfer*, **62**, 109–121.
- Kemppinen O., Nousiainen T., and Jeong, G. Y. (2015). Effects of dust particle internal structure on light scattering. *Atmos. Chem. Phys.*, **15**, 12011–12027.
- Kinne, S., Ackerman, T. P., Heymsfield, A. J., Valero, F. P. J., Sassen, K., and Spinhirne, J. D. (1992). Cirrus microphysics and radiative transfer: Cloud field

- study on 28 October 1996. *Mon. Weather Rev.*, **120**, 661–684, doi:10.1175/1520-0493(1992)120<0661:CMARTC>2.0.CO;2.
- Kinne, S., Ackerman, T. P., Shiobara, M., Uchiyama, A., Heymsfield, A. J., Miloshevich, L., Wendell, J., Eloranta, E., Purgold, C., and Bergstrom, R. W. (1997). Cirrus cloud radiative and microphysical properties from ground observations and in situ measurements during FIRE 1991 and their application to exhibit problems in cirrus solar radiative transfer modeling. *J. Atmos. Sci.*, **54**, 2320–2344, doi:10.1175/1520-0469(1997)054<2320:CCRAMP>2.0.CO;2
- Kinne S., Lohmann, U., Feichter, J., Schulz, M., Timmreck, C., Ghan, S., Easter, R., Chin, M., Ginoux, P., Takemura, T., Tegen, I., Koch, D., Herzog, M., Perner, J., Pitari, G., Holben, B., Eck, T., Smirnov, A., Dubovik, O., Slutsker, I., Tanre, D., Torres, O., Mishchenko, M., Geogdzhayev, I., Chu, D. A., and Kaufman, Y. (2003). Monthly averages of aerosol properties: A global comparison among models, satellite data and AERONET ground data. *J. Geophys. Res.*, **108**(D20), doi:10.1029/2001JD001253a.
- Koop, T., Luo, B., Tsias, A., and Peter, T. (2000). Water activity as the determinant for homogeneous ice nucleation in aqueous solutions. *Nature*, **406**, 611–614.
- Kopp, G. and Lean, J. L. (2011). A new, lower value of total solar irradiance: Evidence and climate significance. *Geophys. Res. Lett.*, **38**, L01706, doi:10.1029/2010GL045777.
- Korolev, A. V. and Isaac, G. A. (2003). Roundness and aspect ratio of particles in ice clouds. *J. Atmos. Sci.*, **60**, 1795–1808.
- Korolev, A. V., Emery, E. F., Strapp, J. W., Cover, S. G., Isaac, G. A., Wasey, M., and Marcotte, D. (2011). Small ice particles in tropospheric clouds: Fact or artifact? *Bull. Amer. Meteor. Soc.*, **92**, 967–973.
- Korolev, A. V., Emery, E., and Creelman, K. (2013). Modification and tests of particle probe tips to mitigate effects of ice shattering. *J. Atmos. Ocean. Tech.*, **30**, 690–708.
- Labonnote, L. C., Brogniez, G., Buriez, J.-C., Doutriaux-Boucher, M., Gayet, J.-F., and Macke, A. (2001). Polarized light scattering by in-homogeneous hexagonal monocrystals. Validation with ADEOS-POLDER measurements. *J. Geophys. Res.*, **106**, 12139–12153.

- Lindqvist, H., Muinonen, K., Nousiainen, T., Um, J., McFarquhar, G. M., Haapanala, P., Makkonen, R., and Hakkarainen, H. (2012). Ice-cloud particle habit classification using principal components. *J. Geophys. Res. Atmos.*, **117**, D16, doi:10.1029/2012JD017573.
- Liou, K.-N. (2002). Introduction to Atmospheric Radiation (2nd Ed.). *Academic Press*, San Diego, 583 pp, ISBN 0-12-451451-0.
- Macke, A. (1993). Scattering of light by polyhedral ice crystals. *Applied Optics*, **32**, 2780–2788.
- Macke, A., Mueller J., and Raschke, E. (1996). Single scattering properties of atmospheric ice crystals. *J. Atmos. Sci.*, **53**, 2813–2815, doi:10.1175/1520-0469(1996)053<2813:SSPOAI>2.0.CO;2.
- Macke A., Francis, P. N., McFarquhar, G. M., and Kinne, S., (1998). The role of particle shapes and size distributions in the single scattering properties of cirrus clouds. *J. Atmos. Sci.*, **55**, 2874–2883.
- Macke, A., Mitchell, D., and Bremen, L. (1999). Monte Carlo radiative transfer calculations for inhomogeneous mixed phase clouds. *Phys. Chem. Earth (B)*, **24**, 3, 237–241.
- Marshak, A. and Davis, A. B. (2005). Radiative Transfer in Cloudy Atmospheres. *Springer Verlag*, pp. 701.
- Mason, B. J. (1992). Snow crystals, natural and man made. *Contemporary Physics*, **33**, 227–243, doi:/10.1080/00107519208223972
- Mayer, B. and Kylling, A. (2005). Technical note: The libRadtran software package for radiative transfer calculations - description and examples of use. *Atmos. Chem. Phys.*, **5**, 1855–1877.
- McFarquhar, G. M. and Heymsfield, A. J. (1997). Parameterization of tropical cirrus ice crystal size distributions and implications for radiative transfer: Results from CEPEX. *J. Atmos. Sci.*, **54**, 2187–2200, doi:10.1175/1520-0469(1997)054<2187:POTCIC>2.0.CO;2.
- McFarquhar, G. M., Heymsfield, A. J., Macke, A., Iaquinta, J., and Aulenbach, S. M. (1999). Use of observed ice crystal sizes and shapes to calculate mean-scattering

- properties and multispectral radiances: CEPEX April 4, 1993, case study. *J. Geophys. Res.*, **104**(D24), 31, 763–31, 779, doi:10.1029/1999JD900802.
- McFarquhar, G. M., Yang, P., Macke, A., and Baran, A. J., (2002). A new parameterization of single scattering solar radiative properties for tropical anvils using observed ice crystal size and shape distributions. *J. Atmos. Sci.*, **59**, 2458–2478.
- McFarquhar, G. M., Um, J., Freer, M., Baumgardner, D., Kok, G. L., and Mace, G. (2007). Importance of small ice crystals to cirrus properties: Observations from the Tropical Warm Pool International Cloud Experiment (TWP-ICE). *Geophys. Res. Letter.*, **34**, L13803, doi:10.1029/2007GL029865.
- McFarquhar, G. M., Baumgardner, D., Bansemmer, A., Abel, S., Crosier, J., French, J., Rosenberg, P., Korolev, A., Schwarzenboeck, A., Leroy, D., Um, J., Wu, W., Heymsfield, A. J., Detwiler, A., Field, P., Neumann, A., Stith, J., Axisa, D., Cotton, R., and Dong, J. (2016). Processing of in-situ data collected by bulk water, scattering and cloud imaging probes: Fundamentals, Uncertainties and Efforts towards consistency. *Amer. Meteor. Soc. Monographs*, Under review, 2016.
- Merikallio, S., Lindqvist, H., Nousiainen, T., Kahnert, M. (2011). Modelling light scattering by mineral dust using spheroids: assessment of applicability. *Atmos. Chem. Phys. D.*, **11**(2), 3977–4016, doi:10.5194/acpd-11-3977-2011.
- Middleton, N. J. and Goudie, A. S. (2001). Saharan dust: sources and trajectories. *Transactions of the Institute of British Geographers*, **26**, 165–181, doi:10.1111/1475-5661.00013.
- Mishchenko, M. I., and Travis, L. D. (1994). T-matrix computations of light scattering by large spheroidal particles. *Opt. Commun.*, **109**, 16–21.
- Mishchenko, M. I., Travis, L. D., Kahn, R. A., and West, R. A. (1997). Modeling phase functions for dustlike tropospheric aerosols using a shape mixture of randomly oriented polydisperse spheroids. *J. Geophys. Res.*, **102**(D14), 16831–16847.
- Mishchenko, M. I., Geogdzhayev, I. V., Liu, L., Ogren, J. A., Lacis, A. A., Rossow, W. B., Hovenier, J. W., Volten, H., Muñoz, O. (2003). Aerosol retrievals from AVHRR radiances: effects of particle nonsphericity and absorption and an updated long-term global climatology of aerosol properties. *J. Quant. Spectrosc. Radiat. Transfer*, **79–80**, 953–972.

- Mitchell, D. L. and Arnott, W. P. (1994). A model predicting the evolution of ice particle size spectra and the radiative properties of cirrus clouds. Part II: Dependence of absorption and extinction on ice crystal morphology. *J. Atmos. Sci.*, **51**, 817–832.
- Mitchell, D. L. (2002). Effective Diameter in Radiation Transfer: General Definition, Applications, and Limitations. *J. Atmos. Sci.*, **59**, 2330–2346, doi: 10.1175/1520-0469(2002)059<2330:EDIRTG>2.0.CO;2.
- Neshyba, S. P., Grenfell, T. C., Warren, S. G. (2003). Representation of a nonspherical ice particle by a collection of independent spheres for scattering and absorption of radiation: II. Hexagonal columns and plates. *J. Geophys. Res.*, **108**(D15), 4448, doi:10.1029/2002JD003302.
- Nousiainen, T. (2009). Optical modeling of mineral dust particles: A review. *J. Quant. Spectrosc. Radiat. Transfer*, **110**, 1261–1279.
- Nousiainen, T. and Kandler, K. (2015). Light scattering by atmospheric mineral dust particles. in Light Scattering Reviews 9, Edit. Kokhanovsky, A. A., *Springer Praxis Books*, Springer, Berlin, doi:10.1007/978-3-642-37985-7
- Nousiainen, T. and McFarquhar, G. M. (2004). Light scattering by quasi-spherical ice crystals. *J. Atmos. Sci.*, **61**, 2229–2248, doi:10.1175/1520-0469(2004)061<2229:LSBQIC>2.0.CO;2.
- Nousiainen, T., Kahnert, M., and Veihelmann, B. (2006) Light scattering modeling of small feldspar aerosol particles using polyhedral prisms and spheroids. *J. Quant. Spectrosc. Radiat. Transfer*, **101**, 471–487.
- Nousiainen, T., Kahnert, M., and Lindqvist, H. (2011). Can particle shape information be retrieved from light scattering observations using spheroidal model particles? *J. Quant. Spectrosc. Radiat. Transfer*, **112**, 2213–2225, doi:10.1478/C1V89S1P070
- Otto, S., Bierwirth, E., Weinzierl, B., Kandler, K., Esselborn, M., Tesche, M., Schladitz, A., Wendisch, M., and Trautmann, T. (2009). Solar radiative effects of a Saharan dust plume observed during SAMUM assuming spheroidal model particles. *Tellus B*, **61**, 270–296, doi:10.1111/j.1600-0889.2008.00389.x.
- Otto, S., Trautmann, T., and Wendisch, M. (2011). On realistic size equivalence and shape of spheroidal Saharan mineral dust particles applied in solar and thermal radiative transfer calculations. *Atmos. Chem. Phys.*, **11**, 11, 4469–4490.

- Petty, G. W. (2006). A First Course in Atmospheric Radiation (2nd Ed.). *Sundog Publishing*, USA, ISBN-10: 0-9729033-1-3.
- Prospero, J. M., Ginoux, P., Torres, O., Nicholson, S. E., and Gill, T. E (2002). Environmental characterization of global sources of atmospheric soil dust identified with the Nimbus 7 total ozone mapping spectrometer (TOMS) absorbing aerosol product. *Rev. Geophys.*, **40**(1), 1002, doi:doi:10.1029/2000RG000095.
- Reinhardt, B., Buras, R., Bugliaro, L., Wilbert, S., Mayer, B., (2014). Determination of circumsolar radiation from Meteosat Second Generation. *Atmos. Meas. Tech.*, **7**, 823–838.
- Roeckner, E., Bäuml, G., Bonaventura, L., Brokopf, R., Esch, M., Giorgetta, M., Hagemann, S., Kirchner, I., Koernblueh, L., Manzini, E., and Rhodin, A., Schlese, U., Schulzweida, U., and Tompkins, A. (2003). The atmospheric general circulation model ECHAM 5. Part I: Model description. Rep. 349, Max Planck Institute for Meteorology, Hamburg, German.
- Roeckner, E., Brokopf, R., Esch, M., Giorgetta, M., Hagemann, S., Koernblueh, L., Manzini, E., Schlese, U., and Schulzweida, U. (2006). Sensitivity of simulated climate to horizontal and vertical resolution in the ECHAM5 atmosphere model. *J. Climate*, **19**, 3771–3791. doi:10.1175/JCLI9023.1.
- Räisänen, P., Järvenoja, S., and Järvinen, H. (2008). Noise due to the Monte Carlo independent-column approximation: short-term and long-term impacts in ECHAM5. *Q. J. R. Meteorol. Soc.*, **134**, 631, 481–495, doi:10.1002/qj.231.
- Schlimme, I., Macke, A., and Reichardt, J. (2005). The impact of ice crystal shapes, size distributions, and spatial structures of cirrus clouds on solar radiative fluxes. *J. Atmos. Sci.*, **62**, 2274–2283.
- Schmitt, C., Schnaiter, M., Heymsfield, A., Yang, P., Hirst, E., and Bansemer, A. (2016). The Microphysical Properties of Small Ice Particles Measured by the Small Ice Detector-3 Probe during the MACPEX Field Campaign. *J. Atmos. Sci.*, **73**, 4775–4791, doi:10.1175/JAS-D-16-0126.1.
- Schmitt, C. G. and Heymsfield, A. J. (2007). On the occurrence of hollow bullet rosette- and column-shaped ice crystals in midlatitude cirrus. *J. Atmos. Sci.*, **64**, 4514–4519, doi: 10.1175/2007JAS2317.1

- Segal-Rosenheimer, M., Russell, P. B., Livingston, J. M., Ramachandran, S., Redemann, J., and Baum, B. A. (2013). Retrieval of cirrus properties by Sun photometry: A new perspective on an old issue. *J. Geophys. Res. Atmos.*, **118**, 4503–4520, doi:10.1002/jgrd.50185.
- Shi, Y. and Long, C. N. (2002). Best estimate radiation flux value-added procedure: Algorithm operational details and explanations. Tech. Rep. DOE/SC-ARM/TR-008, Pac. Northwest Natl. Lab., Richland, Wash.
- Shiobara, M. and Asano, S. (1994). Estimation of cirrus optical thickness from sun photometer measurements. *J. Appl. Meteorol.*, **33**, 672–681, doi:10.1175/1520-0450.
- Simmons, A. J., Burridge, D. M., Jarraud, M., Girard, C., and Wergen, W. (1989). The ECMWF medium-range prediction models development of the numerical formulations and the impact of increased resolution. *Meteorology and Atmospheric Physics*, **40**, 28–60, doi:10.1007/BF01027467.
- Sokolik, I. N. and Toon, O. B. (1999). Incorporation of mineralogical composition into models of the radiative properties of mineral aerosol from UV to IR wavelengths. *J. Geophys. Res.* **104**, 9423–9444.
- Sokolik, I. N., Winker, D. M., Bergametti, G., Gillette, D. A., Carmichael, G., Kaufman, Y. J., Gomes, L., Schuetz, L., and Penner, J. E. (2001). Introduction to special section: Outstanding problems in quantifying the radiative impacts of mineral dust. *J. Geophys. Res. Atmos.*, **106**, D16, 18015–18027, doi:10.1029/2000JD900498
- Stamnes, K., Tsay, S.-C., Wiscombe, W., and Jayaweera, K. (1988). Numerically stable algorithm for discrete-ordinate-method radiative transfer in multiple scattering and emitting layered media. *Appl. Opt.*, **27**, 2502–2509, doi:10.1364/AO.27.002502.
- Stephens, G. L., Tsay, S.-C., Stackhouse, P. W., and Flatau, P. J. (1990). The relevance of the microphysical and radiative properties of cirrus clouds to climate and climatic feedback. *J. Atmos. Sci.*, **47**, 1742–1754, doi:10.1175/1520-0469(1990)047<1742:TROTMA>2.0.CO;2.
- Stier, P., Feichter, J., Kinne, S., Kloster, S., Vignati, E., Wilson, J., Ganzeveld, L., Tegen, I., Werner, M., Balkanski, Y., Schulz, M., Boucher, O., Minikin, A., and Petzold, A. (2005). The aerosol-climate model ECHAM5-HAM. *Atmos. Chem. Phys.*, **5**, 1125–1156. doi:10.5194/acp-5-1125-2005.

- Stubenrauch, C. J., Cros, S., Guignard, A., and Lamquin, N. (2010). A 6-year global cloud climatology from the Atmospheric InfraRed Sounder AIRS and a statistical analysis in synergy with CALIPSO and CloudSat. *Atmos. Chem. Phys.*, **10**, 7197–7214, doi:10.5194/acp-10-7197-2010.
- Takana Y., and Liou, K. N. (1989). Solar radiative transfer in cirrus clouds. Part II: Theory and computation of multiple scattering in an anisotropic medium. *J. Atmos. Sci.*, **46**, 20–36.
- Takano Y. and Liou K. N. (1995). Radiative Transfer in Cirrus Clouds. Part III: Light Scattering by Irregular Ice Crystals. *J. Atmos. Sci.*, **57**, 7.
- Teller, A., Xue, L., and Levin, Z. (2012). The effects of mineral dust particles, aerosol regeneration and ice nucleation parameterizations on clouds and precipitation. *Atmos. Chem. Phys.*, **12**, 9303–9320, doi:10.5194/acp-12-9303-2012.
- Ulanowski, Z., Connolly, P., Flynn, M., Gallagher, M., Clarke, A. J. M., and Hesse, E. (2004). Using ice crystal analogues to validate cloud ice parameter retrievals from the CPI ice spectrometer data. 14th International Conference on Clouds and Precipitation, Bologna, Italy.
- Ulanowski, Z., Kaye, P. H., Hirst, E., Greenaway, R. S., Cotton, R. J., Hesse, E., and Collier, C. T. (2014). Incidence of rough and irregular atmospheric ice particles from Small Ice Detector 3 measurements. *Atmos. Chem. Phys.*, **14**, 1649–1662, doi:10.5194/acp-14-1649-2014.
- Um, J. and McFarquhar, G. M. (2007). Single-scattering properties of aggregates of bullet rosettes in cirrus. *J. Appl. Meteor. Climatol.*, **46**(6), 757–775, doi:10.1175/JAM2501.1.
- Um, J. and McFarquhar, G. M. (2009). Single-scattering properties of aggregates of plates. *Q. J. R. Meteorol. Soc.*, **135**, 291–304, doi:10.1002/qj.378.
- Um, J. and McFarquhar, G. M., (2011). Dependence of the single-scattering properties of small ice crystals on idealized shape models. *Atmos. Chem. Phys.*, **11**, 3159–3171, doi:10.5194/acp-11-3159-2011.
- Um, J., McFarquhar, G. M., Hong, Y. P., Lee, S.-S., Jung, C. H., Lawson, R. P., and Mo, Q. (2015). Dimensions and aspect ratios of natural ice crystals. *Atmos. Chem. Phys.*, **15**, 3933–3956, doi:10.5194/acp-15-3933-2015.

- Vignati, E., Wilson, J., and Stier, P. (2004). M7: An efficient size-resolved aerosol microphysics module for large-scale aerosol transport models. *J. Geophys. Res.*, **109**, D22202, doi:10.1029/2003JD004485.
- Wagner R., Ajtai, T., Kander, K., Lieke, K., Linke, C., Müller, T., Schnaiter, M., and Vragel, M. (2012). Complex refractive indices of Saharan dust samples at visible and near UV wavelengths: a laboratory study. *Atmos. Chem. Phys.*, **12**, 2491–2512, doi:10.5194/acp-12-2491-2012.
- Wang, Z., Zhang, H., Jing, X., and Wei, X. (2013). Effect of non-spherical dust aerosol on its direct radiative forcing. *Atmos. Res.*, **120–121**, 112–126, doi:http://dx.doi.org/10.1016/j.atmosres.2012.08.006.
- Wendisch, M., Pilewskie, P., Pommier, J., Howard, S., Yang, P., Heymsfield, A. J., Schmitt, C. G., Baumgardner, D., and Mayer, B. (2005). Impact of cirrus crystal shape on solar spectral irradiance: a case study for subtropical cirrus. *J. Geophys. Res.*, **110**, D03202, doi:10.1029/2004JD005294.
- Wendisch, M., Yang, P., and Pilewskie, P. (2007). Effects of ice crystal habit on the thermal infrared radiative properties and forcing of cirrus clouds. *J. Geophys. Res.*, **112**, D08201, doi:10.1029/2006JD007899.
- Wiegner, M., Gasteiger, J., Kandler, K., Weinzierl, B., Rasp, K., Esselborn, M., Freudenthaler, V., Heese, B., Toledano, C., Tesche, M., and Althausen, D. (2009). Numerical simulations of optical properties of Saharan dust aerosols with emphasis on lidar applications. *Tellus B*, **61**, 180–194.
- Wylie, D. P. and Menzel, W. P. (1999). Eight years of high cloud statistics using HIRS. *J. Clim.*, **12**, 170–184, doi:10.1175/1520-0442-12.1.170.
- Wylie, D., Darren L., Menzel, W., and Bates, J. (2005) Trends in global cloud cover in two decades of HIRS observations. *Journal of Climate*, **18**, 15, pp.3021–3031.
- Yang, P. and Liou, K. N. (1996). Finite-difference time-domain method for light scattering by small ice crystals in three-dimensional space. *J. Opt. Soc. Am. A*, **13**, 2072–2085.
- Yang, P. and Liou, K. N. (1997). Lights scattering by hexagonal ice crystals: Solution by a ray-by-ray integration algorithm. *J. Opt. Soc. Am. A*, **14**, 2278–2289.

- Yang, P. and Liou, K. N. (1998). Single-scattering properties of complex ice crystals in terrestrial atmosphere. *Contr. Atmos. Phys.*, **71**, 223–248.
- Yang, P., Liou, K. N., Wyser, K., and Mitchell, D. (2000). Parametrization of the scattering and absorption properties of individual ice crystals. *J. Geophys. Res.*, **105**, 4699–4718, doi:10.1029/1999JD900755.
- Yang, P., Baum, B. A., Heymsfield, A. J., Hu, Y. X., Huang, H.-L., Tsay, S.-C., and Ackerman, A. (2003). Single scattering properties of droxtals. *J. Quant. Spectrosc. Radiat. Transfer*, **79–80**, 1159–1169, doi:10.1016/S0022-4073(02)00347-3.
- Yang, P., Feng, Q., Hong, G., Kattawar, G. W., Wiscombe, W. J., Mishchenko, M. I., Dubovik, O., Laszlo, I., and Sokolik, I. N. (2007). Modeling of the scattering and radiative properties of nonspherical dust-like aerosols. *J. Aerosol Sci.*, **38**, 995–1014, doi:10.1016/j.jaerosci.2007.07.001.
- Yang, P., Bi, L., Baum, B. A., Liou, K. N., Kattawar, G. W., Mishchenko, M. I., and Cole, B. (2013). Spectrally consistent scattering, absorption and polarization of atmospheric ice crystals at wavelengths from 0.2 to 100  $\mu\text{m}$ . *J. Atmos. Sci.*, **70**, 330–347.
- Yurkin, M. A., Maltsev, V. P., and Hoekstra, A. G. (2007). The discrete dipole approximation for simulation of light scattering by particles much larger than the wavelength. *J. Quant. Spectrosc. Radiat. Transfer*, **106**, 546–557.
- Yi B., Hsu., C. N., Yang, P., Tsay, S.-C. (2011). Radiative transfer simulation of dust-like aerosols: Uncertainties from particle shape and refractive index. *J. Aero. Sci.*, **42**, 631–644, doi:10.1016/j.jaerosci.2011.06.008
- Yi, B., Yang, P., Baum, B., L’Ecuyer, T., Oreopoulos, L., Mlawer, E., Heymsfield, A., and Liou, K. (2013). Influence of Ice Particle Surface Roughening on the Global Cloud Radiative Effect. *J. Atmos. Sci.*, **70**, 2794–2807, doi:10.1175/JAS-D-13-020.1.
- Zhang Y., Macke, A., and Albers, F. (1999). Effect of crystal size spectrum and crystal shape on stratiform cirrus radiative forcing. *Atmos. Res.*, **52**, 59–75.
- Zhang, K., O’Donnell, D., Kazil, J., Stier, P., Lohmann U., Ferrachat, S., Croft, B., Quaas, J., Wan, H., Rast, S., and Feichter, J. (2012). The global aerosol-climate model ECHAM-HAM, version 2: sensitivity to improvements in process representations. *Atmos. Chem. Phys.*, **12**, 8911–8949, doi:10.5194/acp-12-8911-2012.

Zhou, C., Yang, P., Dessler, A., Hu, Y., and Baum, B. A. (2012). Study of Horizontally Oriented Ice Crystals with CALIPSO Observations and Comparison with Monte Carlo Radiative Transfer Simulations. *J. Appl. Meteor. Climatol.*, **51**, 1426–1439, doi:10.1175/JAMC-D-11-0265.1.